



MISSOURI
S&T

CENTER FOR TRANSPORTATION INFRASTRUCTURE AND SAFETY



A Laboratory Investigation on Three-Sided Structures

by



Abdeldjelil (DJ) Belarbi, Ph.D. and P.E.
Distinguished Professor

Sang-Wook Bae, Ph.D.
Post Doctoral Research Fellow

and



Younmin You, Ph.D.
Visiting Scholar



**NUTC
R227**

**A National University Transportation Center
at Missouri University of Science and Technology**

Disclaimer

The contents of this report reflect the views of the author(s), who are responsible for the facts and the accuracy of information presented herein. This document is disseminated under the sponsorship of the Department of Transportation, University Transportation Centers Program and the Center for Transportation Infrastructure and Safety NUTC program at the Missouri University of Science and Technology, in the interest of information exchange. The U.S. Government and Center for Transportation Infrastructure and Safety assumes no liability for the contents or use thereof.

Technical Report Documentation Page

1. Report No. NUTC R227	2. Government Accession No.	3. Recipient's Catalog No.	
4. Title and Subtitle A Laboratory Investigation on Three-Sided Structures		5. Report Date February 2009	
		6. Performing Organization Code	
7. Author/s A. Belarbi, S. Bae and Y. You		8. Performing Organization Report No. 00022561	
9. Performing Organization Name and Address Center for Transportation Infrastructure and Safety/NUTC program Missouri University of Science and Technology 220 Engineering Research Lab Rolla, MO 65409		10. Work Unit No. (TRAIS)	
		11. Contract or Grant No. DTRT06-G-0014	
12. Sponsoring Organization Name and Address U.S. Department of Transportation Research and Innovative Technology Administration 1200 New Jersey Avenue, SE Washington, DC 20590		13. Type of Report and Period Covered Final	
		14. Sponsoring Agency Code	
15. Supplementary Notes			
16. Abstract Egyptian Concrete Co. has recently developed a three-sided structure that adopts the advantages of both flat-top and arch-top three-sided culverts: (1) more convenient and lower cost of manufacturing flat-top culverts and (2) capability of the relatively long spans of arch-top culverts. The legs and top slab of the three-sided structures have been designed to resist the bending moments and shear forces developed by the following loads: (1) dead load of soil top cover, (2) self-weight, (3) lateral earth pressures and (4) traffic live loads. However, the structural performance of the three-sided structures developed by Egyptian Concrete Co. needs to be evaluated through experimental and analytical investigations before they will be placed into service. Thus, a full-scale three-sided structure was constructed and tested to failure in the High-Bay Structural Laboratory at the Missouri University of Science and Technology (Missouri S&T). Finite element model (FEM) analysis using a commercial non-linear finite element program was also conducted to supplement the experimental work. The results are presented in this report, which includes cracking patterns, deflections, cracking load, ultimate load and reaction forces.			
17. Key Words Bridge, culvert, waterway, three-sided structure	18. Distribution Statement No restrictions. This document is available to the public through the National Technical Information Service, Springfield, Virginia 22161.		
19. Security Classification (of this report) unclassified	20. Security Classification (of this page) unclassified	21. No. Of Pages 63	22. Price

TABLE OF CONTENTS

1. INTRODUCTION	1
2. TEST PROGRAM	3
2.1. Specimen Detail and Preparation.....	3
2.2. Test Setup.....	3
2.3. Instrumentation	7
3. TEST RESULTS AND DISCUSSIONS	10
3.1. Crack Patterns	10
3.2. Shrinkage Cracks	10
3.3. Detensioning	10
3.4. Load Cases 1 and 2	11
3.4.1. Crack Patterns	11
3.4.2. Load and Deflection Relationship	12
3.4.3. Corner Displacement	14
3.4.4. Horizontal Reaction Forces.....	14
3.4.5. Strains in the Reinforcement.....	15
3.5. Load Cases 3	16
3.5.1. Crack Patterns	16
3.5.2. Failure Modes	16
3.5.3. Strains in Reinforcement.....	16
3.5.4. Strains in the Legs and Effects of Horizontal Restraint at the Bottom of the Legs	19
3.5.5. Horizontal Reaction Force	21
3.5.6. Transverse Distribution of the Loading	22
4. FINITE ELEMENT SIMULATION	23
4.1. Introduction.....	23
4.2. Model Geometry and Configuration.....	23
4.3. Analysis Cases	25
4.4. Model Description	26
4.5. Results and Discussion	26
4.5.1. Load-Displacement Relation	28
4.5.2. Crack patterns and Failure Modes	30
4.5.3. Stress Variations on Concrete (Von Mises Stress)	33
4.5.4. Stress Variations in Steel Reinforcement (Principal Stresses)	36
5. CONCLUSIONS.....	38
6. REFERENCES	40
APPENDIX A. SPECIMEN DETAILS	
APPENDIX B. TENSILE TEST RESULTS OF REINFORCING BARS	
APPENDIX C. CRACK PATTERNS	
APPENDIX D. TEST RESULTS OF LOAD CASE 1	
APPENDIX E. TEST RESULTS OF LOAD CASE 2	
APPENDIX F. TEST RESULTS OF LOAD CASE 3	

1. INTRODUCTION

The American Society of Civil Engineers (ASCE), in its 2001 Report Card for America's Infrastructure, gave the nation's infrastructure an average grade of "D+." Since then, things have not improved. The 2005 Report Card gave a grade of "D-" (ASCE, 2005) showing that the infrastructure is continuing to deteriorate. In addition, the Federal Highway Administration (FHWA) reported that approximately 30% of the nation's 589,243 bridges are deficient functionally or structurally and the majority of the structurally deficient bridges are short spans, less than 50 ft in length.

Precast concrete culverts have been used as an economical alternative for replacing short span bridges, less than 20 ft in length. Currently, design standards for four-sided box culverts are provided by American Society for Testing and Materials (ASTM), i.e., ASTM C1433-08 Specifications for Precast Reinforced Concrete Monolithic Box Sections for Culverts, Storm Drains, and Sewers. According to the standards, the maximum span length of standard precast four sided concrete box culvert is 12 ft. However, this maximum length is sometimes too small to treat heavy water flow. Thus, multiple sections of four-sided culverts have to be installed side by side. In this case, the walls of the culverts act as obstacles against the water flow, possibly causing flooding problems. Although precast four-sided culverts with longer spans can be constructed to resolve this problem, the transportation problem still exists due to the increased weight of the culverts as well as transportation width restrictions.

Three-sided precast box culverts have been used as short span bridges that range from 14 ft to 42 ft and are considered an alternative for multiple sections of four-sided precast box culverts. A three sided bridge provides the structural integrity of a box culvert and allows for a natural stream bed with very little impact on the existing waterway and environment. In addition, the three-sided culverts require relatively short installation time and a lower cost when compared to a conventional cast in place bridge system. In general, the three-sided precast concrete culvert system consists of two precast or cast-in-placed concrete footings that are set or cast on a crushed stone bed on each side of the stream. The footings are cast with a keyway on their top surface to receive the legs of the three sided box sections. Three-sided precast concrete culverts can be divided into two main categories: (1) flat top three-sided culverts and (2) arch top three-sided culvert as shown in Figure 1.1.



(a) flat-top (www.americanconcrete.com)



(b) arch-top (Con/Span Bridge © Bridge Systems)

Figure 1.1. Two Types of Three-Sided Precast Box Culverts.

Egyptian Concrete Co. has recently developed a three-sided structure that adopts the advantages of both flat-top and arch-top three-sided culverts: (1) more convenient and lower cost of manufacturing of flat-top culverts and (2) capability of the relatively long spans of arch-top culverts. The legs and top slab of the three-sided structures have been designed to resist the bending moments and shear forces developed by the following loads: (1) dead load of soil top cover, (2) self-weight, (3) lateral earth pressures and (4) traffic live loads. However, the structural performance of the three-sided structures developed by Egyptian Concrete Co. needs to be evaluated through experimental and analytical investigations before they will be placed in service. Thus, a full-scale three-sided structure was constructed and tested to failure in the High-bay Structural Laboratory at the Missouri University of Science and Technology (Missouri S&T). Finite element model (FEM) analysis using a commercial non-linear finite element program was also conducted to supplement the experimental work.

2. TEST PROGRAM

2.1. Specimen Detail and Preparation

The three-sided structure tested at Missouri S&T was 28 ft in span, 8 ft in rise, and 5 ft in lay length and reinforced with Grade 60 mild steel reinforcing bars as shown in Appendix A. The clear cover for reinforcement was maintained at 1.5 in. or 2 in. depending on the locations of reinforcing bars. The legs were inclined at 72 degrees relative to the horizontal. The specimen was constructed by Egyptian Concrete Co. and delivered to the High-bay Structures Laboratory at Missouri S & T.

The concrete strength was measured by testing three cylinders at the day of testing and its compressive strength was 6,500 psi. Three samples of #5 reinforcing bars were tested and the results, including the complete stress-strain relationships, are provided in Appendix B.

2.2. Test Setup

The test specimen was subjected to three different loading cases as shown in Figure 2.1. In Load Case 1, load was applied up to 25 kips which corresponded to a point around the calculated flexural cracking load at a location near the north side leg as shown in Figure 2.1(a). Then, the loading frame was moved to the other loading point near the south side leg and tested in the same manner as shown in Figure 2.1(b). After Load Case 2, the loading frame was placed at the centerline of the test specimen as shown in Figure 2.1(c), and the test specimen was incrementally loaded to failure.

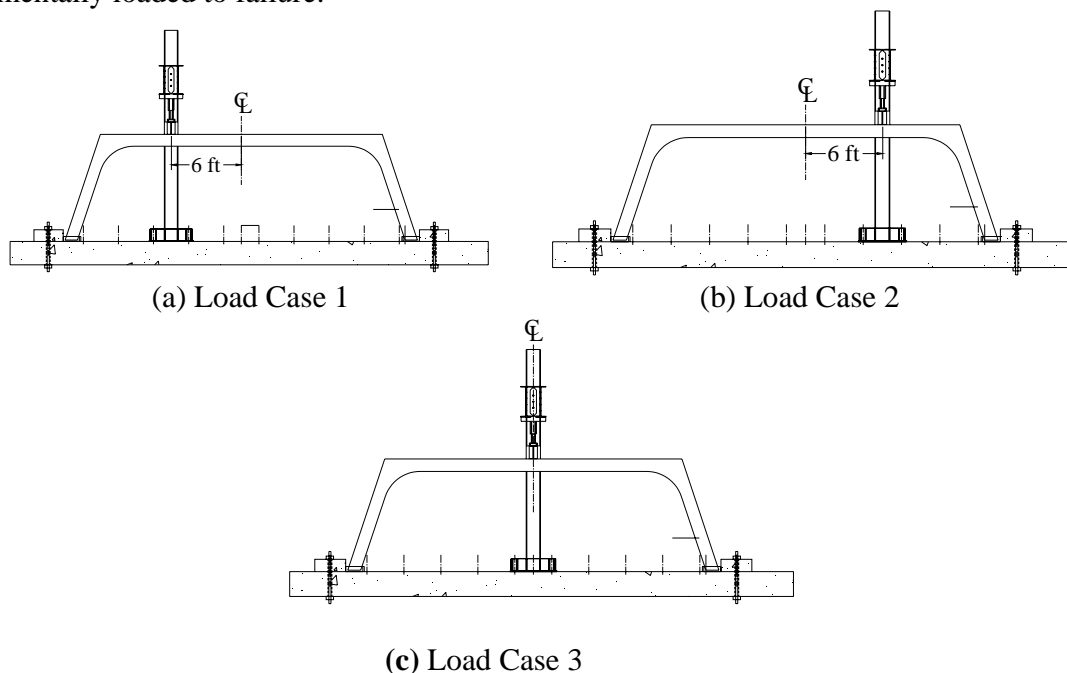
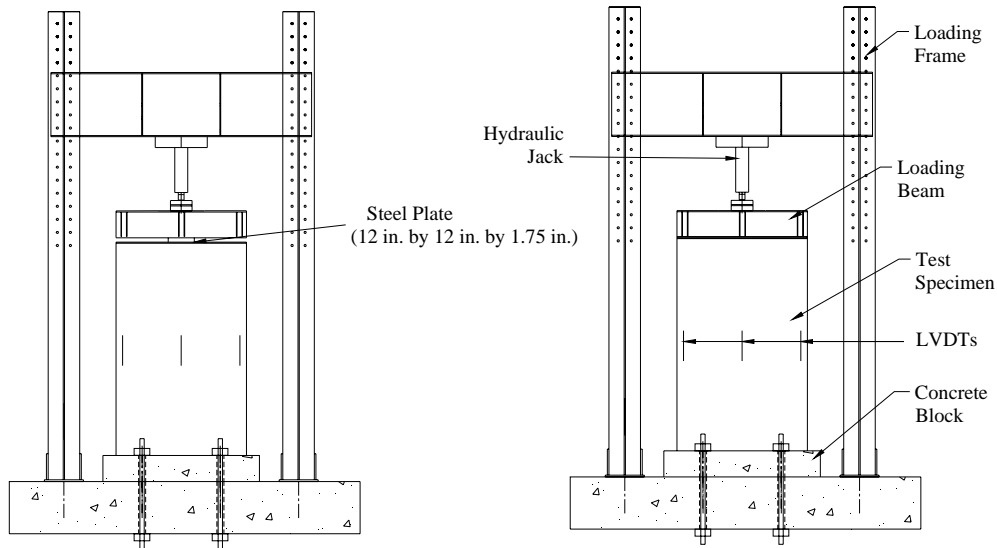


Figure 2.1. Load Cases (West Side View)

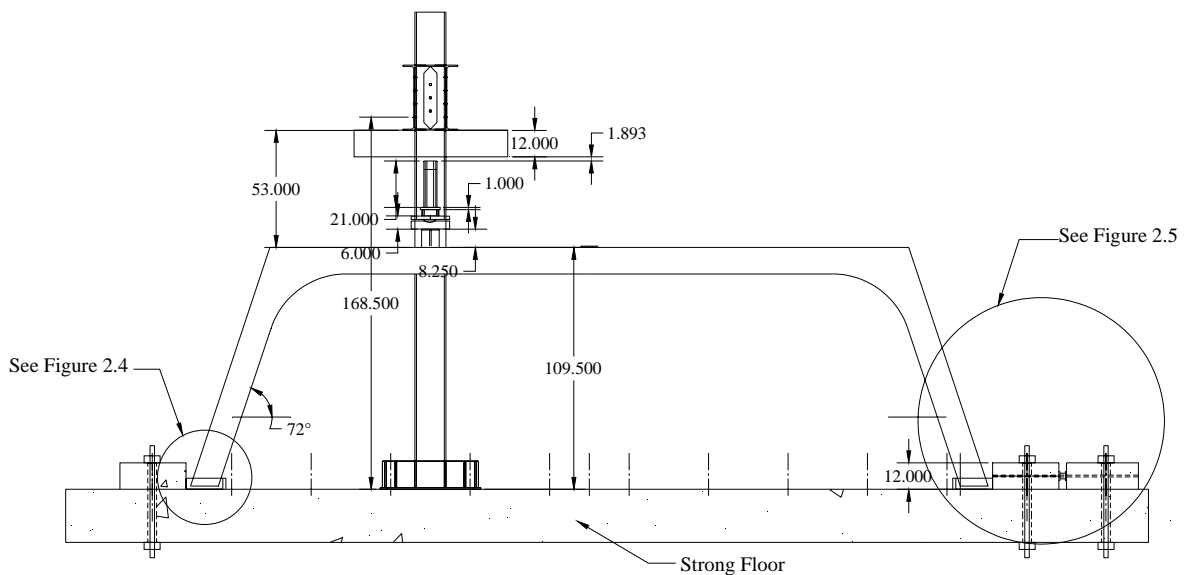
A hydraulic jack of 200 kips capacity was used to apply load and a load cell was placed between the hydraulic jack and the loading beam to monitor the magnitude of applied load as shown in Figure 2.2. The load applied to the specimen for Load Cases 1 and 2 was a line load

across the lay length with an 8 in. width, as shown in Figure 2.2(b), while Load Case 3 used a concentrated load at the center of the deck. The concentrated load was applied through a 1.75 in. thick steel plate (12 in. by 12 in.) inserted between the loading beam and the test specimen as shown in Figure 2.2(a). Figure 2.3 shows a photograph taken during testing while the test specimen was being subjected to Load Case 3.



(a) South Side View for Load Case 3

(b) South Side View for Load Cases 1 and 2



(c) West Side View for Load Cases 1 and 2

Figure 2.2. Test Set-up



Figure 2.3. Photo of the Test in Progress

The typical installation of three-sided structures in the field requires a strip footing with a 3 in. deep recess or keyway. The legs of three-sided structure units are placed into the recess and leveled with shims. Then, the gap between the leg and recess is grouted. The strip footings and grouting was simulated as shown in Figure 2.2(c). The details of this procedure for the north side leg were depicted in Figure 2.4; while Figure 2.5 presents the details for the south side. As shown in Figure 2.4, a concrete block was first secured on the strong floor with a prestressing force of 75 kips applied to two Dywidag Bars to provide the horizontal restraint. Four small wooden blocks, 1 3/4" in thickness, were then placed between the strong floor and the leg. Then, formworks for grouting were installed and the grout was cast. Hydrostone^{TR} was used for the grouting material.

The procedure for the south side leg was similar to that used for the north side except that two concrete blocks were used instead of just one concrete block. The space between the two blocks provided a means to measure the horizontal reaction forces as shown in Figure 2.5. The procedure was as follows: (1) four layers of plastic sheeting were placed over the area on which the south side leg, grout and the first concrete block would be placed. The plastic sheets were used to reduce friction between the strong floor and the grout and concrete block. (2) The first concrete block was secured to the strong floor with a prestressing force of 75 kips. (3) The leg was placed and the grout was cast in the same way as described for the north leg. (4) The second concrete block was placed on the strong floor and load cells were inserted in between the first and second concrete blocks. (5) The second concrete block was pushed against the first concrete block with a fork lift so that the gaps between the load cells and the concrete blocks were eliminated. (6) The second concrete block was secured to the strong floor with a prestressing force of 75 kips applied to two Dywidag Bars. (7) The prestressing force applied to the first concrete block was released. In this way, it was assumed that the first concrete block and grouted area on the north side would be fixed against outward horizontal movement and the horizontal reaction forces could be measured using the two load cells to the south. Figure 2.6 shows a picture of the concrete blocks and the load cells.

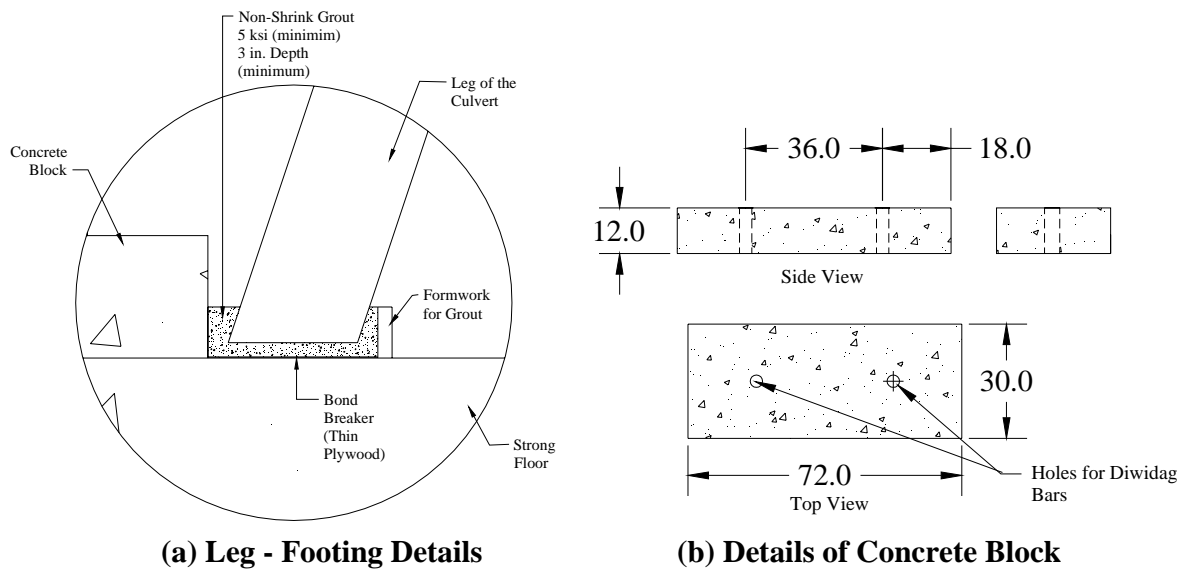


Figure 2.4. Details of the Procedure to Simulate the Grout Between the Legs and Footing in the Laboratory (North Side)

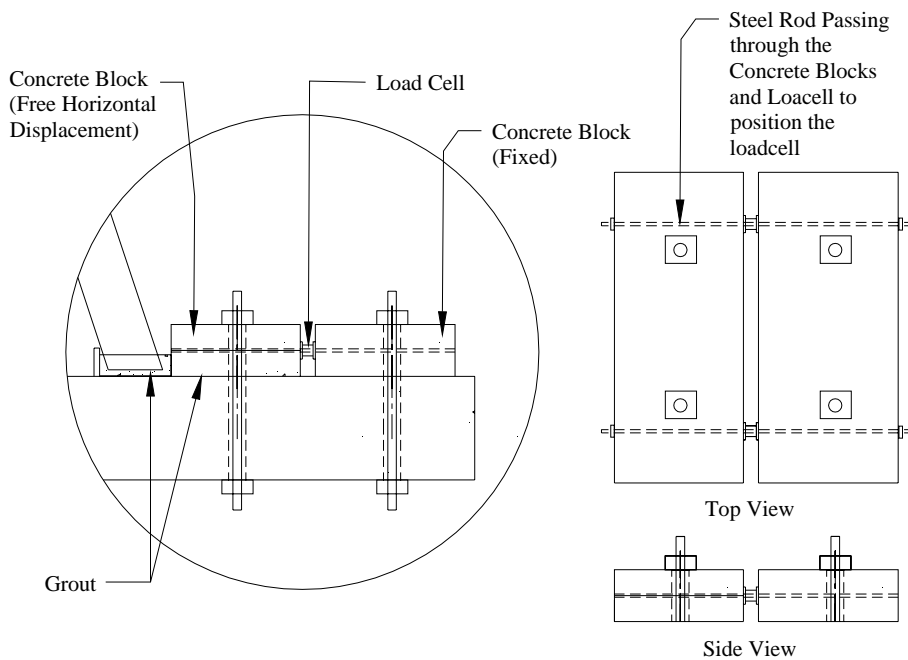


Figure 2.5. Details of the Procedure to Simulate the Grout Between the Legs and Footing in the Laboratory (South Side) and to Measure Horizontal Reaction

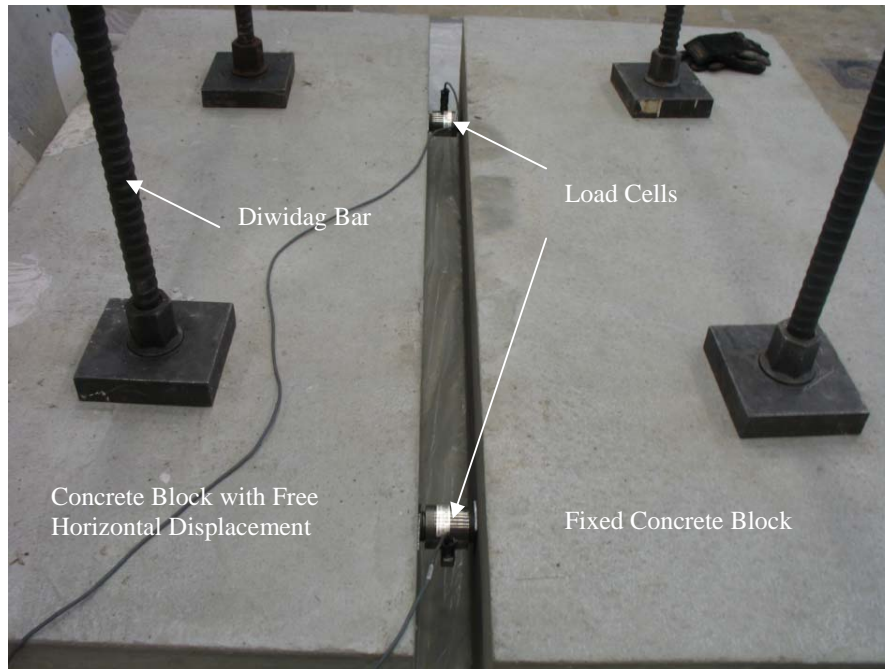


Figure 2.6. Photo of Concrete Block Assembly in the North Side

2.3. Instrumentation

Electric resistance strain gages were installed on multiple locations of reinforcing bars in order to monitor strain levels in the reinforcement. The strain gage locations are shown in Figure 2.7 and they were denoted using letters and numbers. T-series gages were installed to monitor the strains in the top reinforcement while B-series gages were installed for the strains in the bottom reinforcement. The locations of strain gages with numbers 3, 4, and 5 corresponded to the loading points of each load cases (T-3W and B-3W for Load Case 1, T-5W and B-5W for Load Case 2, T-4W and B-4W for Load Case 3). The strain gages installed near the haunches were denoted by numbers, 1, 2, 6, and 7). In addition, each series of gages were installed at three different locations along the lay length of the unit. For example, Strain Gages T-1W and B-1W series were installed near the west side of the three-sided structure while, T-1M, B-1M and T-1E, B-1E were placed in the middle and east side respectively in terms of the lay length.

Vertical and horizontal deformations were also measured using Linear Variable Displacement Transducers (LVDTs) at various locations as shown in Figure 2.8. LVDTs N-X and N-Y were installed in the north haunch region to monitor horizontal and vertical deformations, respectively. LVDTs S-X and S-Y were installed in the south haunch region to monitor horizontal and vertical deformations, respectively. LVDTs DW-N, DW-M, and DW-S were located at the loading points of the three load cases along the west side of the specimen. Although it is not depicted in the figure, LVDTs DM-N, DM-M, and DM-S were also installed along the middle line in terms of the lay length of the unit; while LVDTs DE-N, DE-M, and DE-S were installed along the east side in terms of the lay length of the unit.

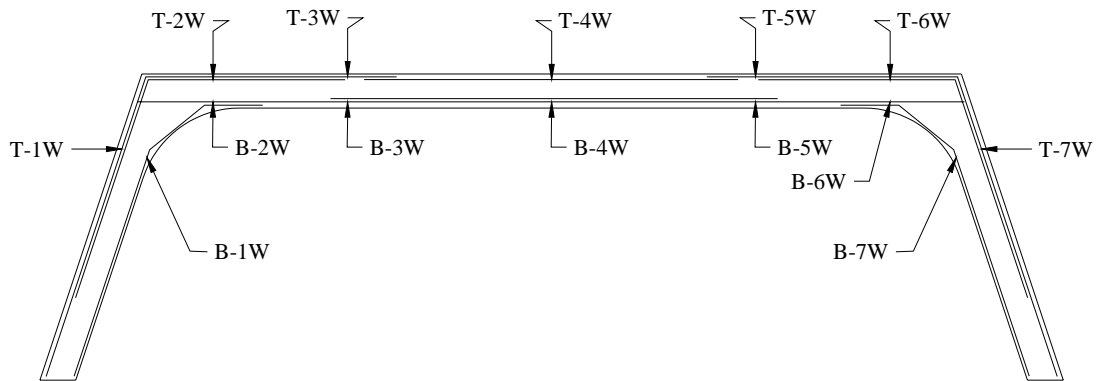


Figure 2.7. Locations of Strain Gages (West Side)

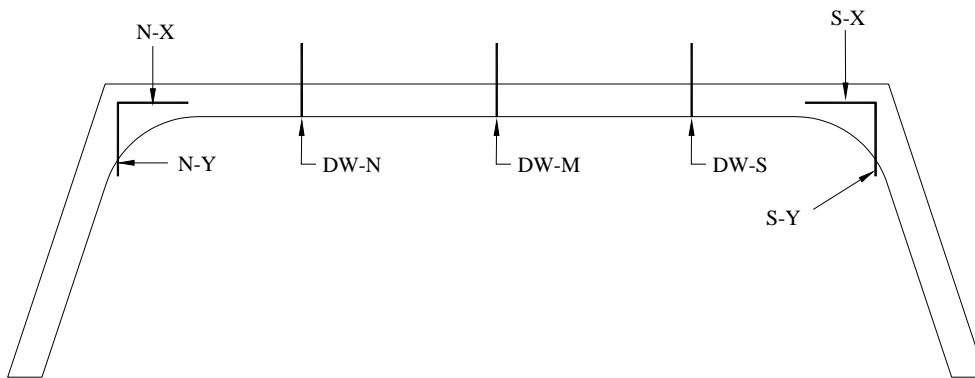


Figure 2.8. Locations of LVDTs and String Transducers (West Side)

LVDTs were installed on each side of both legs to monitor strains and deflections of the legs. Figure 2.9 shows the locations of LVDTs installed on the North leg. LVDTs NW-E, NW-M, and NW-W were placed on the east, middle and west sides of the leg, respectively; while LVDT NW-INS was located on the inside surface of the leg opposite NW-M. LVDT NW-LAT was installed to monitor the deflection of the north leg perpendicular to the leg slope. The same number of LVDTs were installed on the south leg but were denoted SW.

The horizontal movements of the concrete blocks were also monitored with LVDTs. Figure 2.10 shows the locations of LVDTs to measure the horizontal movements of the concrete block on the south side. Two LVDTs were attached to each side (i.e., LVDTs S-CE-W and S-CB-E for the west and east sides of the concrete block, respectively), 1 in. from the outside of the concrete block as shown in Figure 2.10. The concrete block in the north side was instrumented with two LVDTs in a similar manner. The LVDTs on the concrete block at the north side were denoted N-CE-W and N-CB-E.

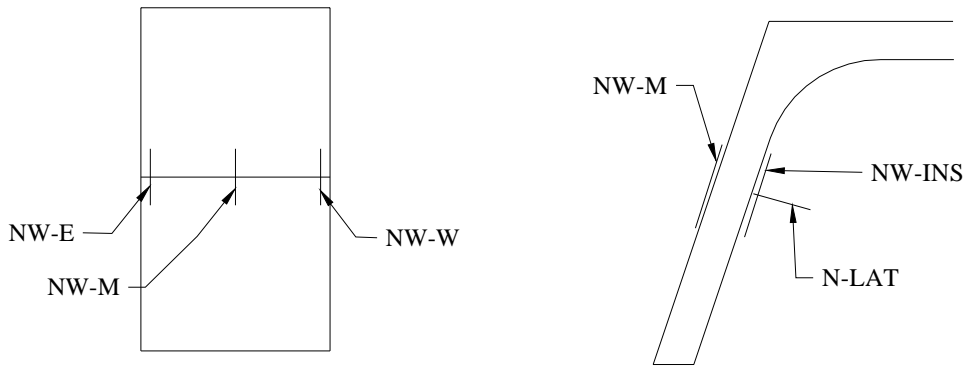


Figure 2.9. Locations of LVDTs on the North Side Leg

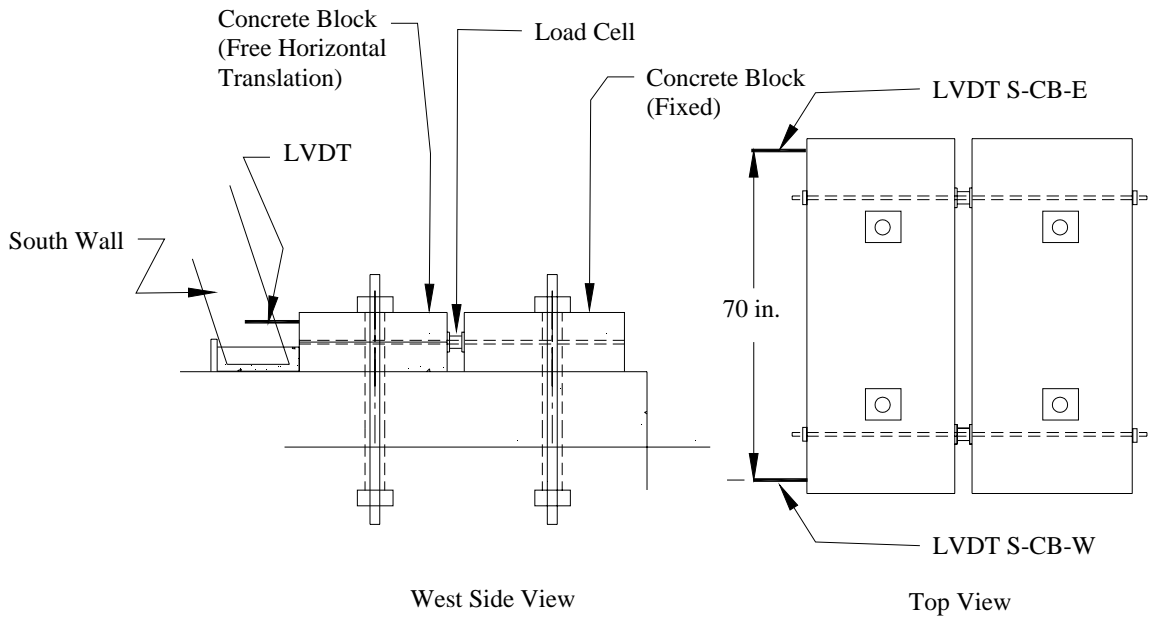


Figure 2.10. Locations LVDTs to Measure Horizontal Movement

3. TEST RESULTS AND DISCUSSIONS

3.1. Crack Patterns

Before and during the testing of the three-sided structures, cracks were marked in different colors for each load case including shrinkage cracks. A complete set of drawings for the crack patterns of all load cases are provided in Appendix C. Discussions on the crack patterns observed during the tests will be made in the main body of this report; however the crack pattern drawings in Appendix C will be referred to when necessary for the purposes of discussion.

3.2. Shrinkage Cracks

Before the test began, the existing cracks, which were considered to be shrinkage cracks, were found and are shown in Figures C.1(a), C.2(a) and C.3(a) in Appendix C. As shown in the figures, most cracks were found near the mid-span of the slab with some near the lifting anchors on the east side of the test specimen. The spacing between the cracks on the bottom surface of the slab was less than the thickness of the slab and the maximum spacing of the shrinkage and temperature reinforcement in the slab, both of which were 12 in.

3.3. Detensioning

The test specimen was constructed at a plant operated by Egyptian Concrete Co. and delivered to the High-bay Structures Laboratory at Missouri S&T with 0.5 inch nominal diameter, 7-wire prestressing strand between the inclined legs to keep them from sliding or spreading during transportation and handling as shown in Figure 3.1. After the legs were placed on the strong floor and grouted with the concrete blocks (see Figures 2.4 and 2.5), the prestressing force of the strand was released as the cramps at one end of the strand was loosened.



Figure 3.1. Handling of the Test Specimen in the Laboratory showing the Prestressing Strand Connected between the Two Inclined Legs

During the detensioning process, the strain variation of the strand was monitored with two LVDTs attached to the strand. The strain values then were used to calculate the prestressing force released during the detensioning process. For calculation purposes, the area of the strand was taken as the nominal area, 0.153 in^2 and the elastic modulus was taken as 27,500 ksi. Meanwhile, the horizontal reaction force created during the detensioning process was measured with the two load cells at the south side leg of the test specimen (see Figure 2.5 for more detail). The results were compared in Figure 3.2. As shown in Figure 3.2, the measured prestressing force released by the strand was 1.56 and 1.61 kips for LVDTs 1 and 2, respectively; while the measured horizontal reaction force reached 1.56 kips. Thus, it can be said that the entire prestressing force was transferred to the horizontal reaction force and that the plastic sheets used to reduce the friction force between the strong floor and the grout / concrete block assembly worked very well.

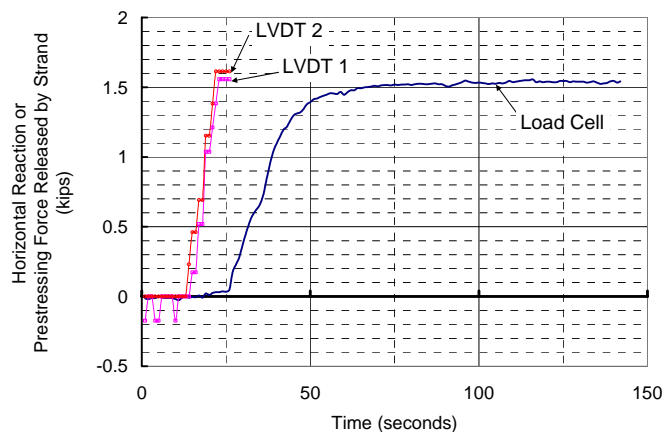


Figure 3.2. Horizontal Reaction Force Caused by Detensioning

From Figure 3.2, it is interesting to note that there was a time delay of 50 seconds between the release of the prestressing force and when the horizontal reaction force reached the maximum value. This could be due to the fact that the load cells used to measure the horizontal reaction forces needed some time to be completely seat and engage in between the two concrete blocks.

3.4. Load Cases 1 and 2

Load Cases 1 and 2 dealt with the a line load applied along the entire width of the slab (see Figures 2.1 and 2.2 for more detail). Load Case 1 was applied at the north side of the test specimen and then, Load Case 2 was applied at south side. For both cases, the load was applied up to 25 kips which was estimated to be around the calculated flexural cracking load of the test specimen.

3.4.1. Crack Patterns

Cracks were marked at each load step, i.e., 5, 10, 15, 20 and 25 kips of loading and the obtained crack patterns are provided in Figures C.1(b), C.2(b) and C.3(b) for Load Case 1 and Figures C.1(c), C.2(c) and C.3(c) for Load Case 2 in Appendix C.

For Load Case 1, new cracks were found and marked on the bottom side of the slab even at the lower level of loading from 5 to 20 kips. These new cracks seemed to be existing

shrinkage cracks which were invisible before applying load. As the load was applied to the test specimen, those invisible shrinkage cracks began to open wider and became perceptible to the eye. Similar observation was also made for Load Case 2.

Just after 20 kips of loading, the first true flexural cracks were observed on the bottom side of the slab and the edges as well for both Load Cases. Thus, it can be said that the flexural cracking load of the test specimen was approximately 20 kips. This observation can be evidenced by the load and deflection relationship which will be discussed in more detail in the next section.

3.4.2. Load and Deflection Relationship

As loads were applied, deflections were measured with LVDTs at three different locations along the width of the slab, i.e., DW-series for the west side of the slab, DE-series for the east side and DM-series for middle of the slab. In each series of LVDTs, three LVDTs were placed at three different locations across the span of the slab, that is, the north and south side loading points and the mid-span of the slab, which were denoted with N, S or M at the end of the names of each LVDT as shown in the following figures in this section (see Figure 2.8 for more detail). Figures 3.3 and 3.4 present the load vs. deflection graphs obtained from those LVDTs for Load Cases 1 and 2, respectively.

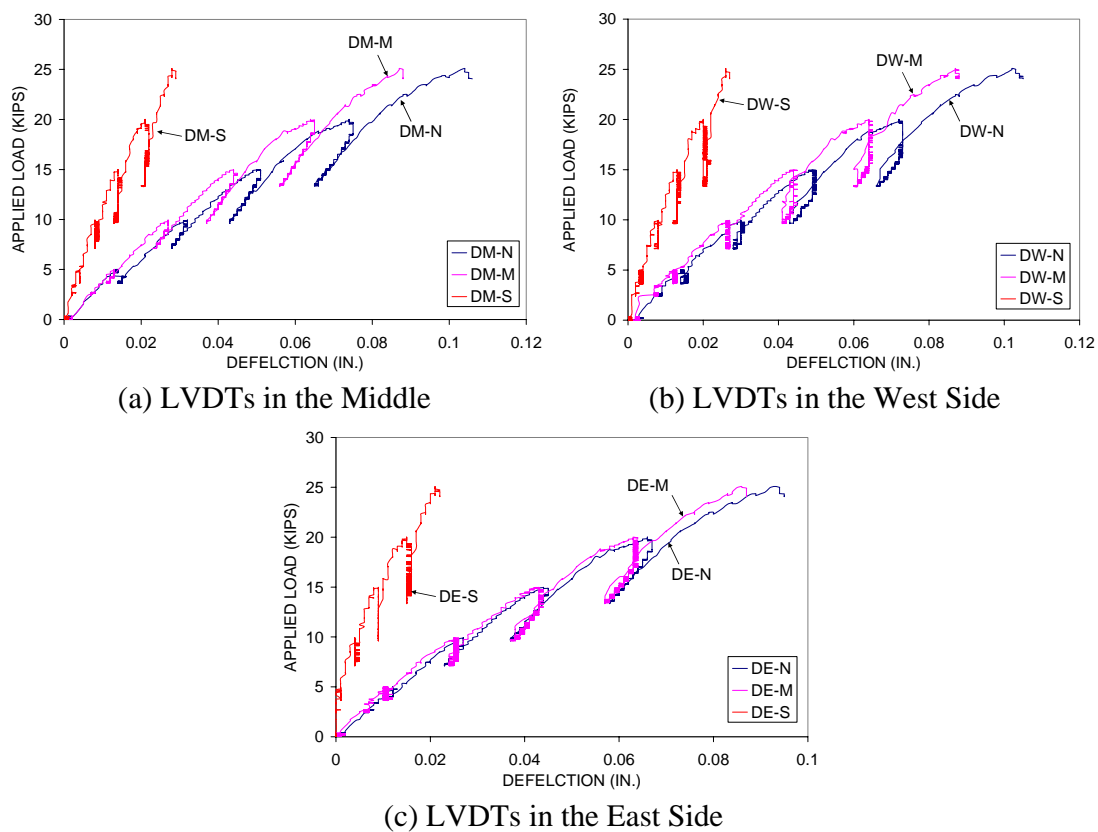


Figure 3.3. Deflections in the Slabs Due to Load Case 1

According to the figures, it is apparent that the deflections were highest at the loading points and became smaller with the increase in distance from the loading points. These figures also show that the deflections at the three different locations across the width of the section, i.e., the east and west side, and the middle of the slab, were nearly the same at every loading step.

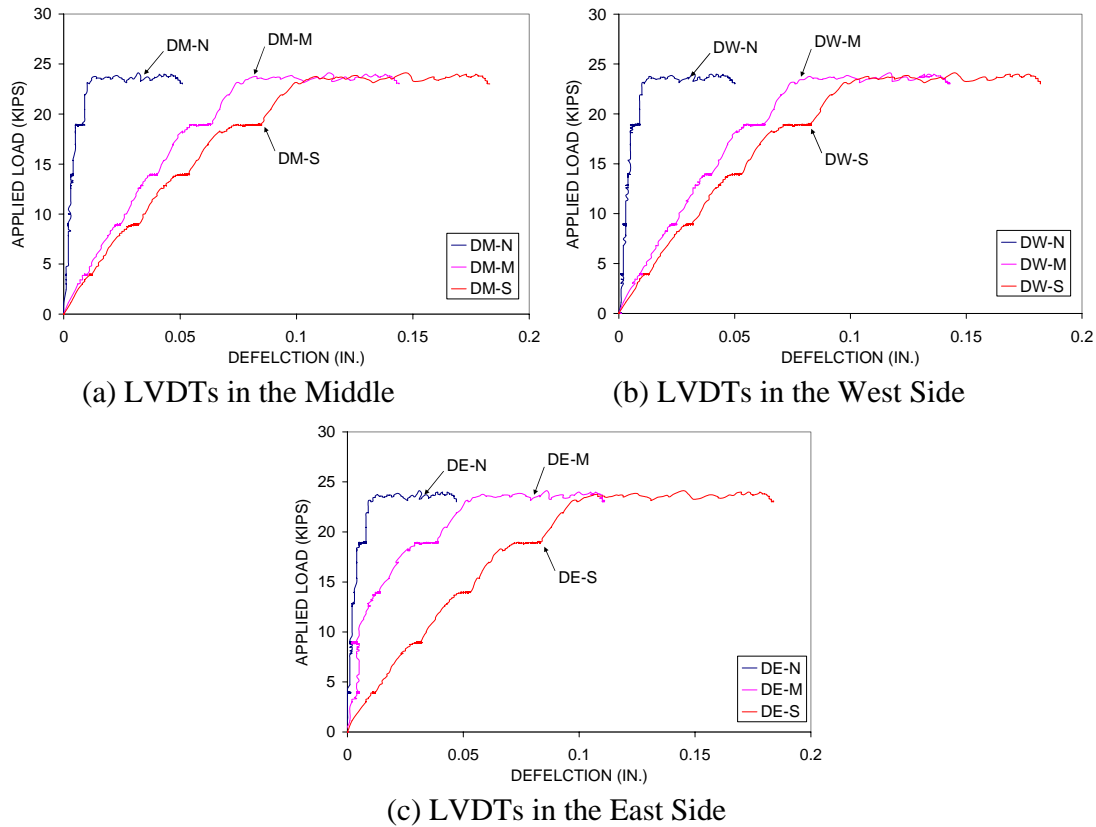


Figure 3.4. Deflections in the Slabs Due to Load Case 2

Figure 3.5(a) shows that the deflections at the loading points of both load cases, i.e., the deflection curve for Load Case 1 in the figure represents the deflections measured with LVDT DM-N while the deflection curve for Load Case 2 represents LVDT DM-S. As shown in Figure 3.5(a), the maximum deflections were 0.12 in. and 0.18 in. for Load Cases 1 and 2, respectively. In addition, it was exhibited that the deflections due to Load Case 2 were slightly higher than those due to Load Case 1 at every load step. This could be a result of some minor damage that occurred in the test specimen during Load Case 1; and thus the flexural stiffness of the test specimen during Load Case 2 was slightly smaller than that of Load Case 1. This phenomenon can be shown more clearly in Figure 3.5(b), which compares the deflections along the span length for both load cases. It can also be noticed from Figure 3.5(b) that for both load cases the deflection increment between 20 kips and 25 kips were greater than the deflection increments between other loading steps (i.e., 0 to 5 kips, 5 to 10 kips, 10 to 15 kips, and 15 to 20 kips). This implies that the stiffness of the test specimen has slightly decreased between loads of 20 and 25

kips, due to the flexural cracking as discussed in the previous section. The slight change of the stiffness of the test specimen at around 20 kips can also be observed in Figure 3.5(a).

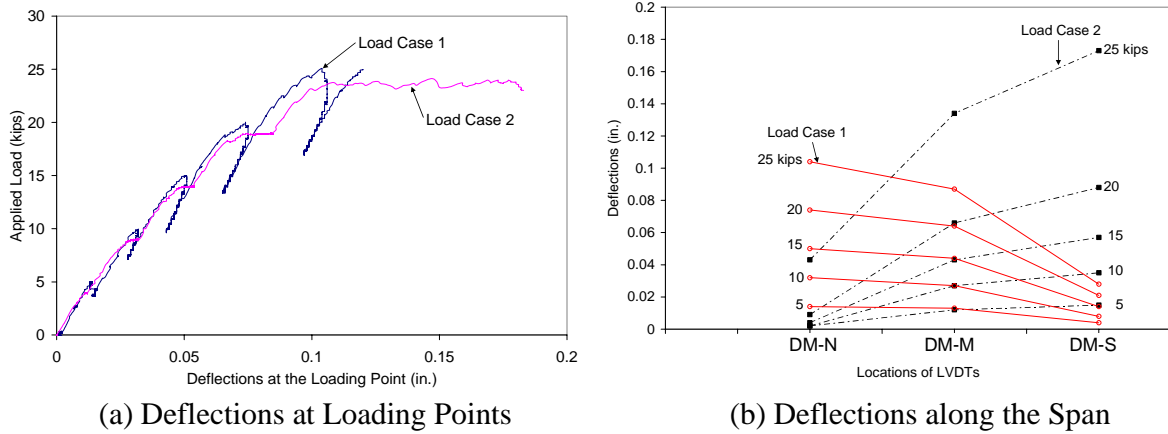


Figure 3.5. Comparisons of Load vs. Deflection Relationship between Load Cases 1 and 2

In addition, it was observed that in Load Case 1 the applied load would drop by about 5 kips in between load steps as shown in Figure 3.5(a). To avoid this during Load Case 2, a small amount of additional hydraulic pressure had to be continuously supplied to the hydraulic jack in order to keep the load constant. Thus, the applied load vs. deflection curves of Load Cases 1 and 2 were slightly different. From Figure 3.5(a), it was noticed that the deflection increased while the applied load was maintained at about 25 kips in the case of Load Case 2 while Load Case 1 did not show such increase in deflection. This could be due to the fact that the existing cracks kept opening while maintaining a constant load near the flexural cracking capacity of the test specimen. However, the increase in deflection resulting from the constant load was just 0.07 in. and can be easily ignored when considering the entire behavior of the test specimen.

3.4.3. Corner Displacement

The horizontal and vertical displacement of a point in the north and south corners of the specimen were monitored with 2 LVDTs installed at each corner (see Figure 2.8 for more detail). Since the applied load was not very significant as compared to the ultimate failure load, the movement of the point was minimal as shown in Figure 3.6, especially in the horizontal direction.

3.4.4. Horizontal Reaction Forces

The horizontal reaction forces were measured at the south side concrete block assembly using two load cells (see Figure 2.5 for more detail) and the obtained results are presented in Figure 3.7. As shown in Figure 3.7, the total horizontal reaction force, sum of Load Cells 1 and 2, was linearly proportional and reached slightly greater than 8.0 kips which was about 32% of the maximum applied load of 25 kips.

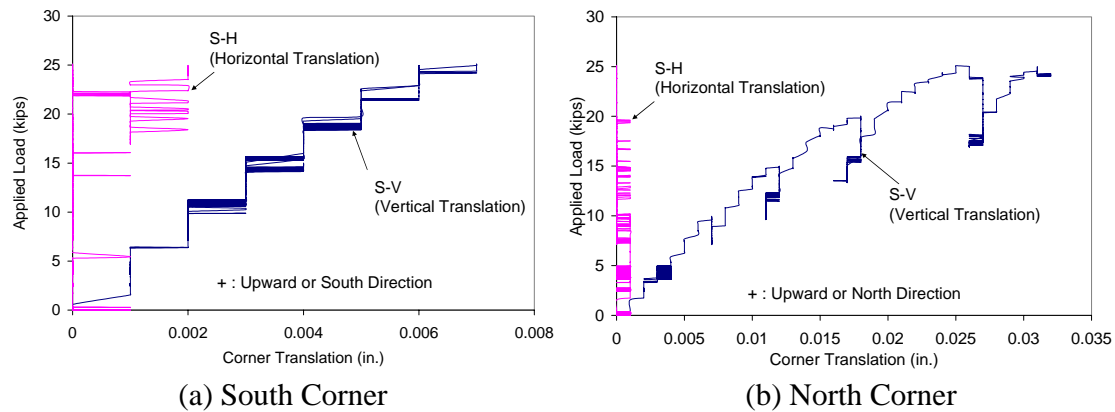


Figure 3.6. Corner Translation

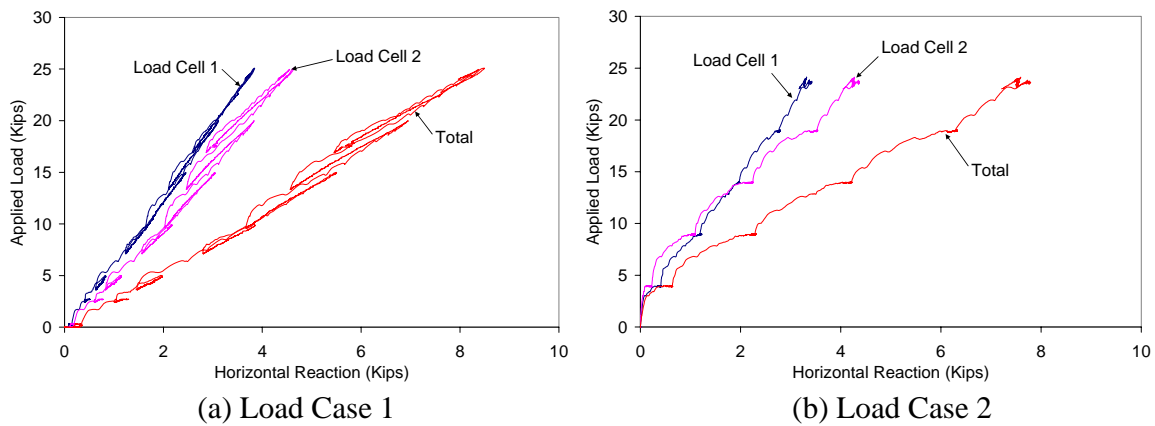


Figure 3.7. Horizontal Reaction Forces

3.4.5. Strains in the Reinforcement

Strains in the reinforcement were measured with the strain gages installed at various locations throughout the reinforcement cage. Figure 3.8 shows the strains in the reinforcement at the loading points (T-3 and B-3 series in Load Case 1, and T-5 and B-5 series in Load Case 2). As shown in Figure 3.8, the strains in the tensile reinforcement (measured with B-series strain gages) were much less than the yield strain although the strains in Load Case 2 were slightly greater than those in Load Case 1. This could be again due to the minor damage that resulted from Load Case 1, which made the test specimen slightly more flexible. The strains in the reinforcement at other locations were minimal. The applied load vs. strain relationship in the reinforcement at other locations for Load Cases 1 and 2 can be found in Appendix D and E, respectively.

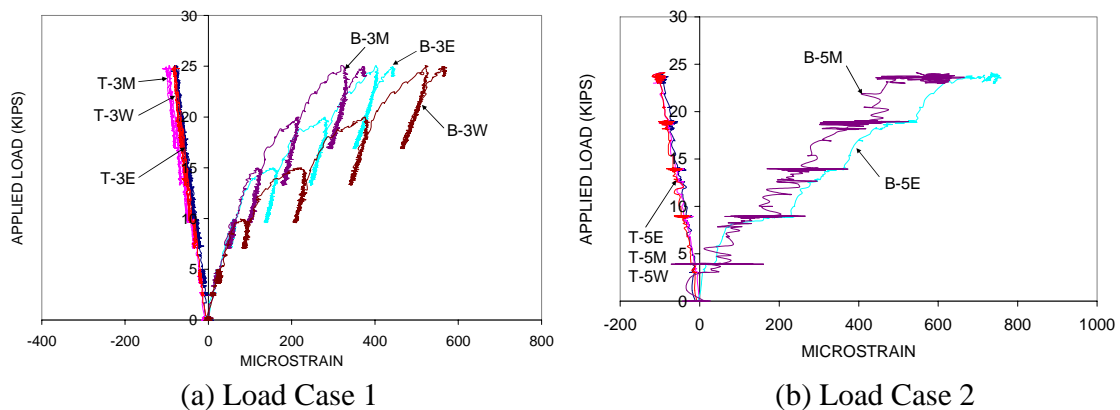


Figure 3.8. Strains in the Reinforcement at the Loading Points

3.5. Load Cases 3

In Load Case 3, the test specimen was loaded with a concentrated load distributed over a 12 in. by 12 in. area to failure, while Load Cases 1 and 2 applied line loads of up to 25 kips. The behavior of the test specimen under Load Case 3 is discussed in this section.

3.5.1. Crack Patterns

As the load was applied beyond the flexural cracking load, many new flexural cracks developed. The crack patterns for Load Case 3 can be found in Figures C.1(d), C.2(d), C.3(d), and C.4(d) of Appendix C. The cracks were observed mostly on the bottom side of the slab near the mid-span due to the positive moment, on the top side of the slab near the haunches, and on the top outside surfaces of the legs near the haunches due to the negative moment. Considering the number of cracks as well as the depth of the cracks, it seemed that the effects of the negative moment was more significant on the top outside of the legs than on the top side of the slab near the haunches as shown in Figure 3.9. This can also be evidenced by the strains in the reinforcement which will be discussed later in this section.

3.5.2. Failure Modes

The yielding of the tensile reinforcement at the mid-span of the slab occurred at about 70 kips of applied load and 1.0 in. of the deflection. Beyond this load, the test specimen underwent a large deflection of up to 5.3 in., and eventually failed due to concrete crushing at the top of the slab at mid-span. Failure occurred at 107 kips of applied load as shown in Figure 3.10. Figure 3.11 presents the photos taken after the failure of the test specimen, and clearly shows the concrete crushing at the top of the slab.

3.5.3. Strains in Reinforcement

For the positive moment region, both Strain Gages B-4M and B-4E were placed on the tensile reinforcement at the mid-span of the slab with Strain Gage B-4M located just under the concentrated load and Strain Gage B-4E located on the reinforcement in the east side of the slab. From Figure 3-12(a), it can be observed that the tensile reinforcement directly under the concentrated load yielded first at 70 kips (see B-4M in Figure 3-12), which corresponds to the large deflection noted in the previous section. Then, the yielding of the reinforcement gradually

spread toward the outer edges of the slab; Strain Gage B-4E yielded at 81 kips while Strain Gage B-4M yielded at 70 kips. Strain Gage B-4W must have been damaged during specimen manufacture since no strain measurements were gathered.

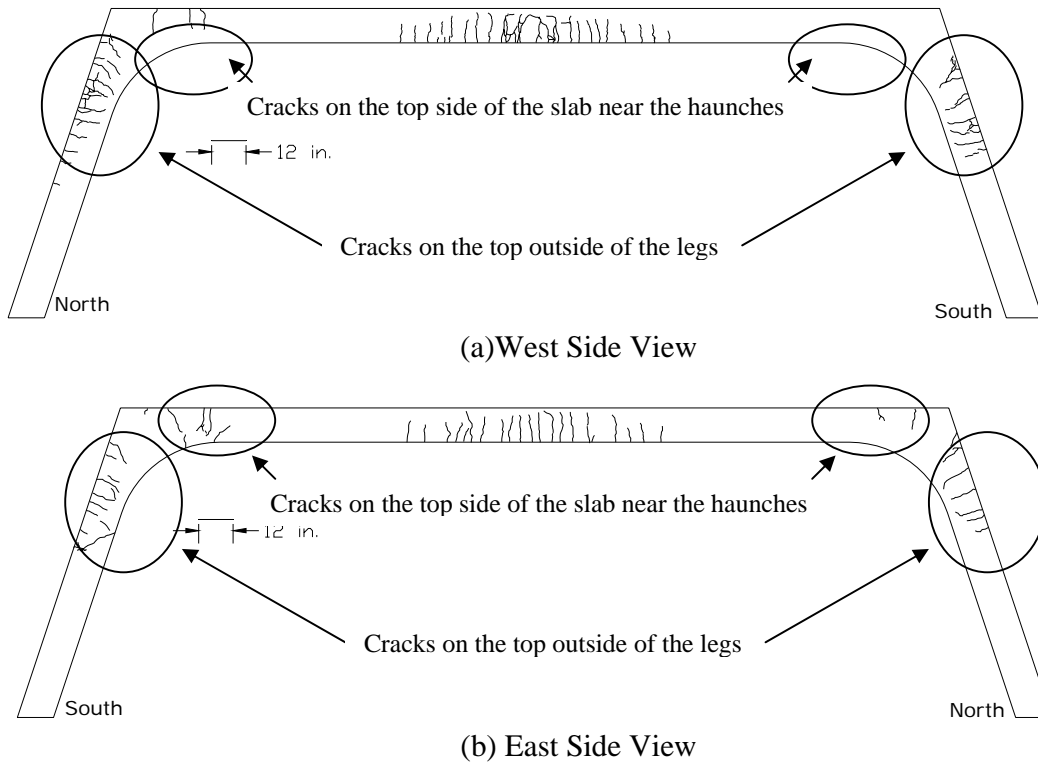


Figure 3.9. Crack Patterns for the Sides of the Test Specimen

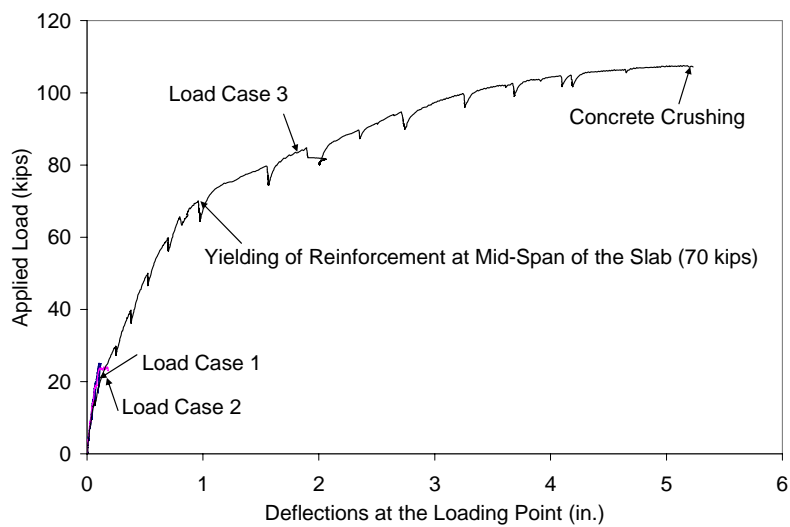
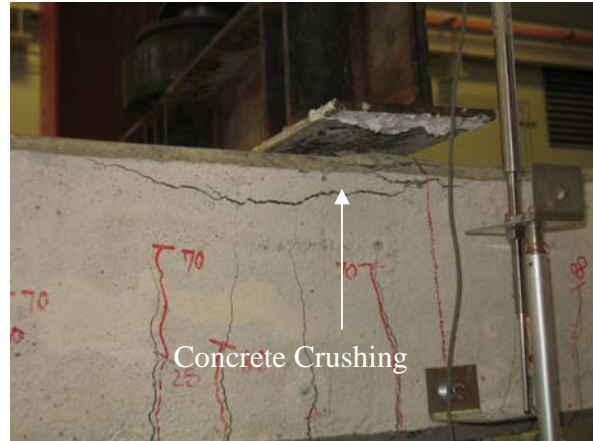


Figure 3.10. Applied Load vs. Deflection Curves

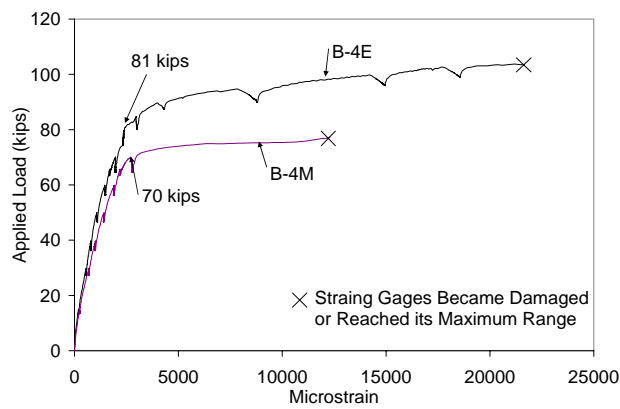


(a) Failed Specimen

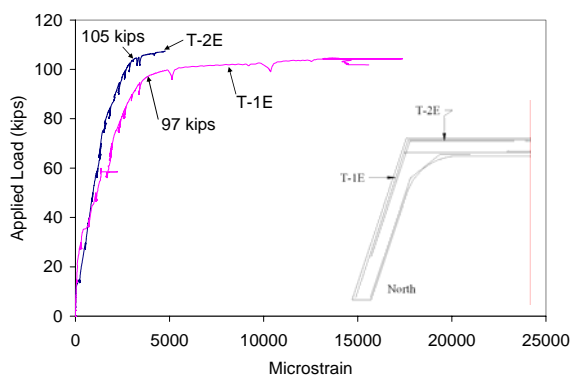


(b) Close-up of the Concrete Crushing

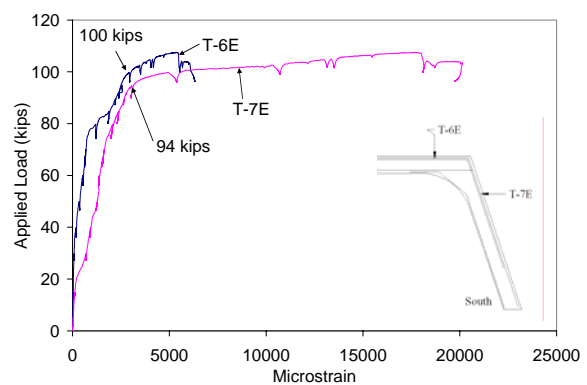
Figure 3.11. Photos Taken after the Failure of the Test Specimen



(a) At mid-span



(b) North Side



(c) South Side

Figure 3.12. Strains in Reinforcement Due to Load Case 3

For the negative moment regions, Strain Gages T-1E and T-2E were installed on the tensile reinforcement in the top outside of the north leg and the top side of the slab near the north haunch, respectively. Strain Gages T-6E and T-7E were installed on the tensile reinforcement in the top side of the slab and in the top outside of the south leg near the south haunch. The measurements from those strain gages were plotted in Figures 3-12(b) and 3-12(c). According to the figures, the tensile reinforcement in the top outside of the legs yielded first at about 96 kips of loading and then the tensile reinforcement in the top side of the slab near the haunches yielded at about 103 kips of loading. This corresponds with the observed crack patterns in which the effects of the negative moment were greater on the top outside of the legs than on the top side of the slab.

Strain gages were also installed in the reinforcement near the cutoff points, 6 ft away from the centerline of the slab. The cutoff point can be an inflection point where the positive moment changes to the negative moment. Strain Gage B-3E was installed near the cutoff point in north side while Strain Gage B-5E was installed similarly in the south side. Figure 3-13 shows the strains measured from those strain gages. As shown in Figure 3-13, the strains of both strain gages increased until the yielding of reinforcement in the mid-span of the slab occurred. After that, the strains started decreasing. This implies that the inflection points in the north and south side of the slab were being shifted toward the strain gage locations after the yielding of the reinforcement at the mid-span of the slab.

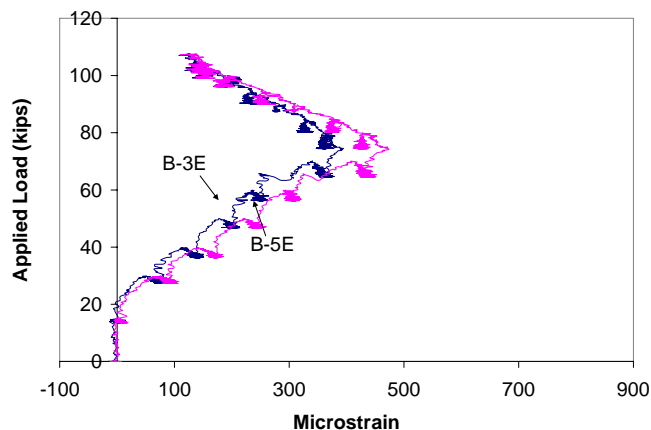


Figure 3.13. Strains of Reinforcement at Cutoff Points

3.5.4. Strains in the Legs and Effects of Horizontal Restraint at the Bottom of the Legs

In previous sections, the discussions were made with the focus on the flexural behavior of the slabs and the regions near the haunches. This section deals with the flexural behavior of the legs by investigating the strains measured with LVDTs at the mid-height of the legs. The LVDTs attached to the inside and outside of the legs had a gage length of 18 in and bridged over several cracks depending on their locations (see Figure 2.9 for more detail). Thus, the strains measured with these LVDTs would represent the average strains. Figure 3.14 shows the measured strains for both legs. As shown in Figure 3.14., the insides of the legs were compressed and the maximum compressive strains were less than 0.001 for both legs at the time of failure of the test specimen, while the outsides of the legs were subjected to tensile stresses and the maximum

tensile strains at the time of failure were 0.0016 and 0.0027 for the south and north legs, respectively. It should be noted, however, that the strains shown in Figure 3.14 do not represent either strains on the surface of concrete or strains in the reinforcement. As shown in Figure 3.15, LVDTs were attached to the legs and the locations of the LVDTs were about 1 in. above the concrete surface. Thus, the actual average tensile strains in the reinforcement would be significantly smaller than the strains measured with the LVDTs, which can be calculated based on the strain compatibility condition. The calculated maximum average tensile strains at the time of failure of the test specimen were 0.0010 and 0.0017 for the south and north legs, respectively. Therefore, it can be said that the reinforcement below the mid-height of the inclined legs would not yield during the entire loading history of the test specimen.

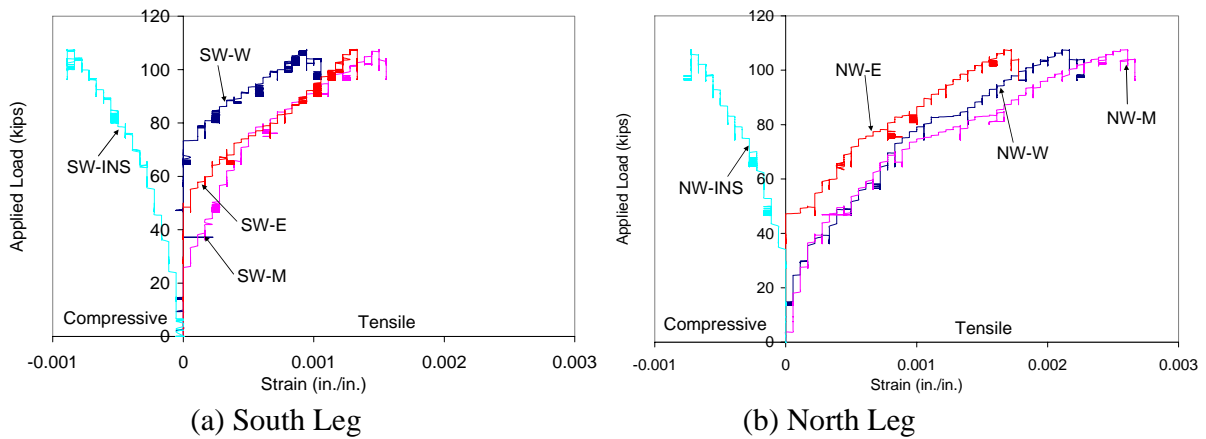


Figure 3.14. Strains in the Mid-Height of the Legs

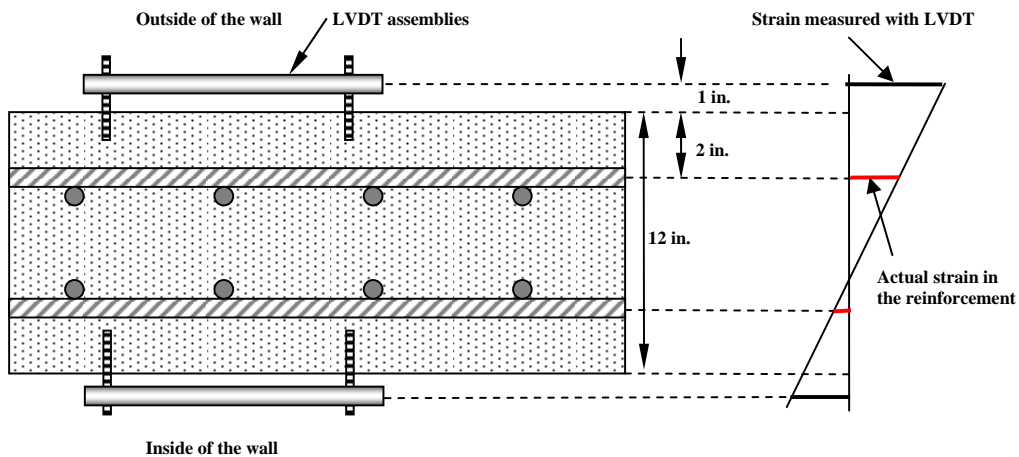


Figure 3.15. Strain Measurement in the Legs with LVDTs

It should be also noticed from Figure 3.14 that the average tensile strains of the north leg were about 60% higher than those of the south leg. In order to find the reasons for the difference, the horizontal movements of the concrete blocks used to provide the horizontal restraint for the legs are investigated. One LVDT was attached at both the west and east side of each concrete block, respectively as shown in Figure 2.10. For the south side concrete block, one LVDT located at the west side was denoted S-CB-W and the LVDT located at the east side was denoted S-CB-E. Similarly, for the north side the LVDTs were denoted N-CB-W and N-CB-E. Then, the horizontal movements of the centerline of the concrete blocks were calculated using the two LVDTs located at the west and east side of the concrete block and identified as ‘AVERAGE’ in Figure 3.16. As shown in Figure 3.16, the average horizontal movement of the south side concrete block was about 0.34 in., while that of the north was 0.034 in. That is, the horizontal restraint provided to the south side leg was not as rigid as the horizontal restraint provided to the north side leg. As a result, the moment in the south side leg should be smaller than that of the north side leg. Note that the tensile strains measured from the LVDTs were also smaller in the south side leg than in the north side leg.

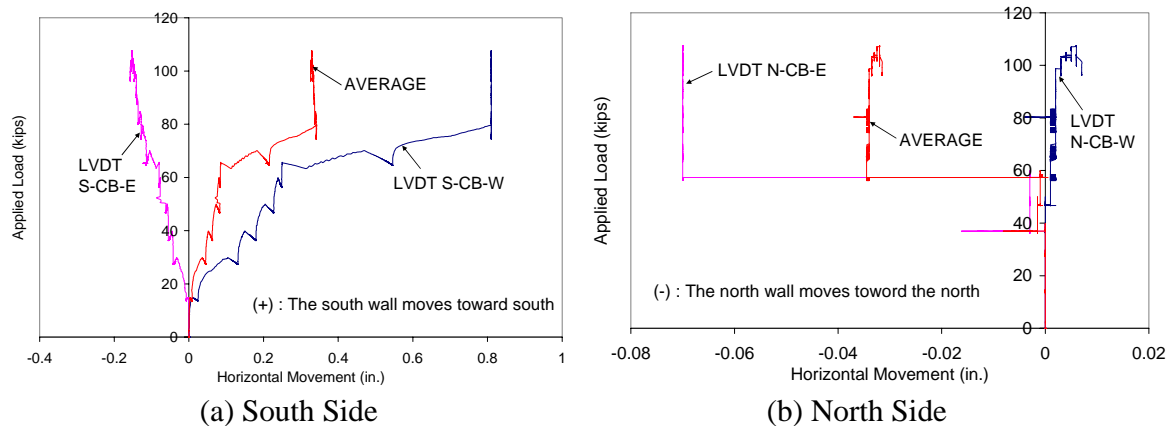


Figure 3.16. Horizontal Movement of the Concrete Block Assemblies at the Side of the Legs

In addition, it was also observed from Figure 3.16 that both legs were twisted instead of moving together in one direction, especially in the case of the south side leg. However, the rotation angle calculated using the maximum values of LVDTs S-CE-W and S-CE-E, shown in Figure 3.16(a), and the geometries shown in Figure 2.10, appeared to be 0.8 degrees which appears to be negligible.

3.5.5. Horizontal Reaction Force

The horizontal reaction forces were measured at the south side concrete block assembly using two load cells (see Figures 2.5 and 2.6 for more detail) and the obtained results are presented in Figure 3.17. As shown in Figure 3.17, the total horizontal reaction force, sum of Load Cells 1 and 2, was linearly proportional and reached 15.9 kips which was about 32% of the applied load of 50 kips. This result is identical to the observation on the horizontal reaction force variation in Load Cases 1 and 2. However, after 50 kips of applied load, the measured horizontal reaction forces became less than 32% of the applied load since the lead sheets and steel washers installed at each side of the load cells were deformed so severely that the load applied to the concrete

blocks could not be properly transferred to the load cells. For example, at 60 kips of loading, the horizontal reaction force was 16.4 kips, 27% of the applied load. Thus, the measurement of the horizontal reaction force was terminated at 60 kips.

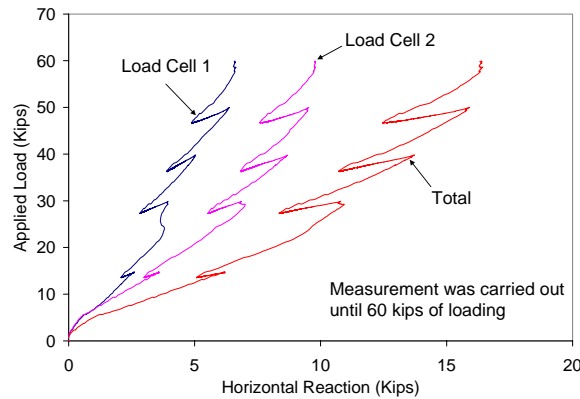


Figure 3.17. Horizontal Reaction Force vs. Applied Load Curves

3.5.6. Transverse Distribution of the Loading

The deflections were also measured across the mid-span of the slab, i.e., one in the middle (LVDT DM-M) and one each in the west and east side of the slab (LVDTs DM-W and DM-E). Figure 3.18 shows the deflections of each measurement point at three different loading steps (20, 40 and 80 kips) and it can be seen from the figure that the concentrated load (12 in. by 12 in.), which simulated a wheel load, could be distributed evenly across the transverse direction of the slab even after the yielding of the tensile reinforcement that occurred at 70 kips. If the service load is considered as 70% of the load at yielding, or 50 kips, the deflection at that load would be 0.56 in. (refer to Figure 3.10), which is less than maximum permissible computed deflections specified in Section 9.5.2.6 of ACI 318-05 ($L/480$ and $L/280$ in.) but greater than the requirement specified in Article 2.5.2.6.2 in AASHTO LRFD specifications ($L/800$).

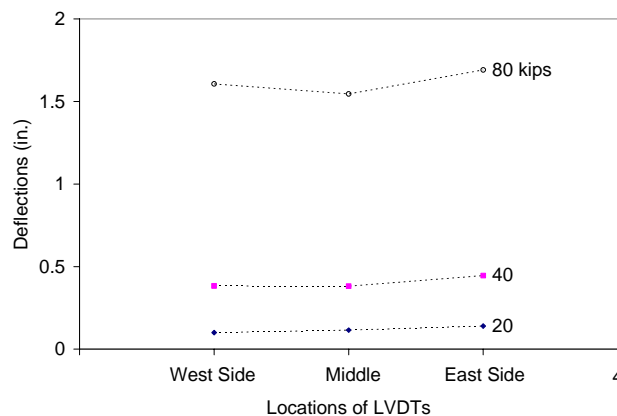


Figure 3.18. Deflections across the Mid-Span of the Slab

4. FINITE ELEMENT SIMULATION

4.1. Introduction

Inelastic finite element (FE) model simulations were carried out to predict the behavior of the test specimen prior to testing and to investigate the local behaviors of the test specimen which can not be investigated through experimental means. For this purpose, a commercial finite element analysis (FEA) software package was used to analyze three-dimensional models of the test specimen. The FEA program is a powerful program that not only has its own large library of structural elements and constitutive material models, but also includes a user defined option where specific elements and constitutive models can be added to the program by users if necessary. This allows maximum flexibility for modeling. The software also has an additional special built-in option, the so-called phased analysis technique, which makes it possible to predict the response of FE model with respect to the time-dependent behavior of elements or material properties. A phased analysis is comprised of several calculation phases. Between each phase, the finite element model is updated by the addition or removal of elements and constraints. In each phase, a separate analysis is performed in which the results from the previous phases are automatically used as initial values. Thus, this technique enables simulating the exact behavior of the test specimen according to test loading history using non-linear analysis.

In this project, two FE models were developed, each with different loading and boundary conditions, in order to simulate the construction environment. The first FE model utilized fixed restraints for the boundary conditions before the test for preliminary analysis and prediction of test specimen behavior. Each loading step was simulated respectively in the analysis. After testing, this FE model was modified to correlate more closely with the observed behavior of the specimen during testing. Major modifications to the model were; i) adopting the exact material properties for the concrete and steel reinforcement from material tests; ii) changing the fixed restraints to pinned restraints in the boundary regions; iii) modeling the boundary regions with stiff elements for simulating the real test set-up and preventing the local failure within this region; iv) simulating the exact test loading history by using a phased analysis. Finally, the analytical results are compared with the experimental results including various analytical features of the software which would be difficult to determine from the experimental results.

4.2. Model Geometry and Configuration

There were several changes in the geometrical aspects of the FE model between the first and second series of analyses. The most significant change was in the change of the boundary conditions. In the first FE model, fixed constraints are applied to the entire bottom surface of the support region without any changes to the element properties in this region as shown in Figure 4.1(a). After testing, significantly different local behavior within the supporting region was observed between the analytical and experimental results. These differences will be explained in the following section. The noted phenomenon forced a change of the boundary conditions for the second FE model. More detailed and realistic considerations when compared to the test results were added into the second FE model. Formerly fixed constraints were changed to pinned conditions along the middle line of the bottom support surfaces and a high stiffness material property was given to the end of supporting region as shown in Figure 4.1(b). Modeling the support surfaces in this way prevents a local failure in the constraint nodes and better simulates the real test set-up configurations. Figure 4.1(c) shows the detailed reinforcement arrangement modeled in both FE models. This reinforcement configuration matches the

reinforcement in the test specimen and eliminates lumped reinforcement that is prevalent using other analytical techniques.

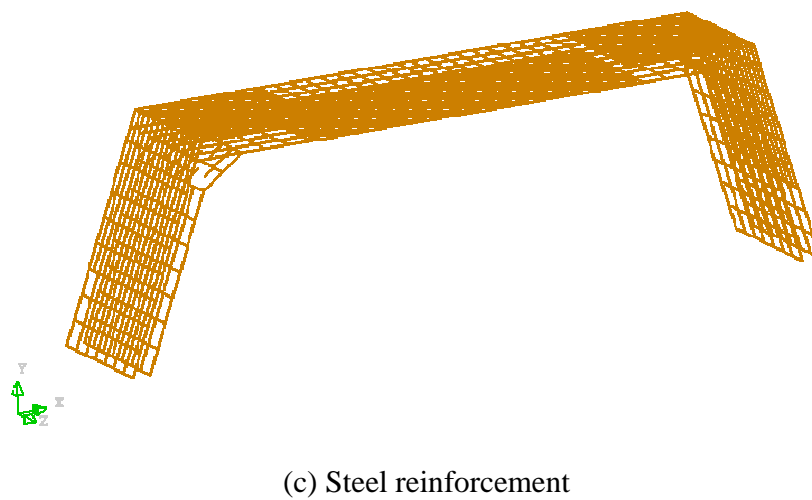
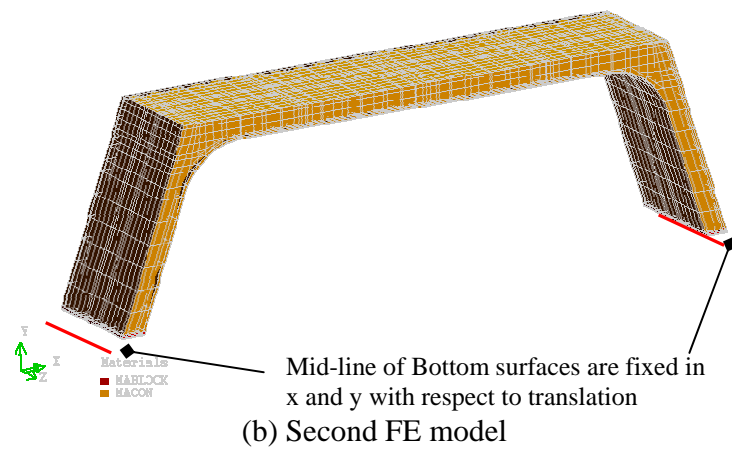
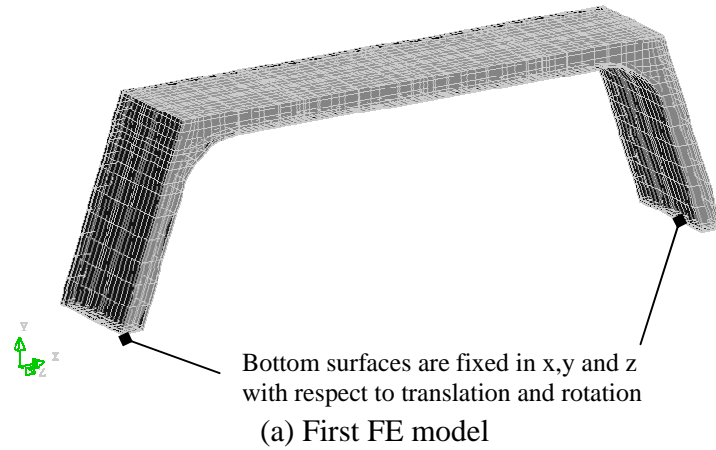


Figure 4.1. Configuration of FE Models

4.3. Analysis Cases

As in the experimental portion of the project, three load cases were applied to the FE models. Two load cases used a line load, which was applied to the test specimen with a steel beam offset 6ft in both directions from the mid-span of the slab. The magnitude of the total applied load was near the calculated cracking load of the test specimen. Following these two load cases, a concentrated load was applied at the center of test specimen in incrementally increased until failure. In the first FE model, load was applied up to failure for the first two load cases using displacement control for prediction. Because these load cases were symmetric and not interdependent, only one simulation was carried out. A concentrated load was also applied up to failure using displacement control. Figure 4.2. shows the analysis cases for the first FE model.

Unlike the first FE model, the load cases applied to the second FE model were exactly the same as the experimental load cases. For the two line loads, load was applied in 5 kip increments up to a total of 25 kips. After these first two load cases, a point load incrementally applied until the analysis came to a halt using the displacement control. In addition, a phase analysis technique was applied to simulate the phased state of the test specimen under a time dependent loading history as shown in Figure 4.3.

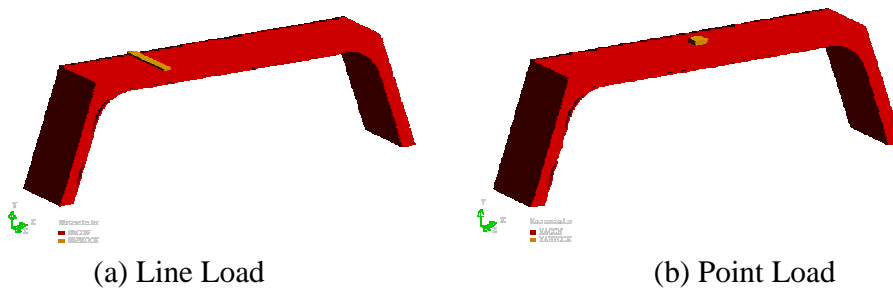


Figure 4.2. Load Cases in the First FE Model

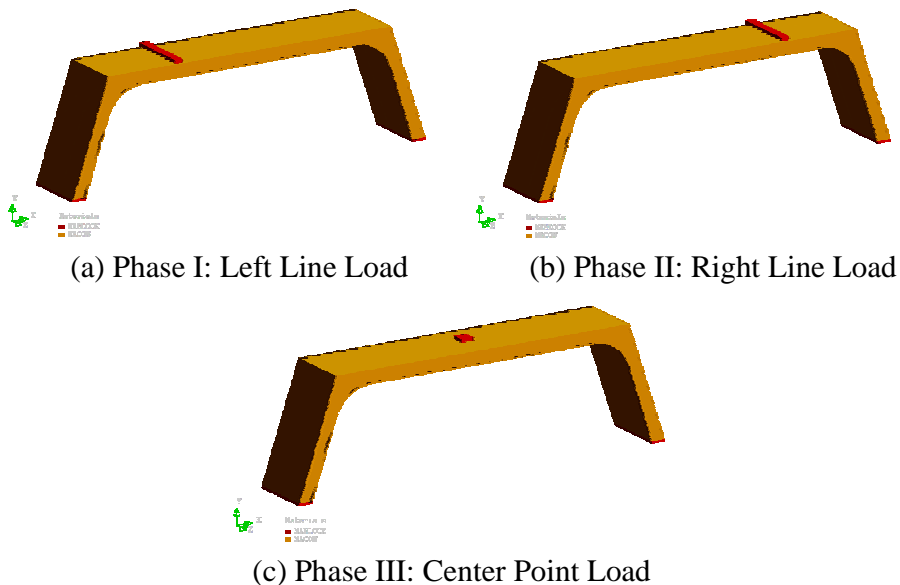


Figure 4.3. Load Cases in the Second FE Model

4.4. Model Description

Detailed views of the FE model are illustrated in Figure 4.4. The eight-node isoparametric solid brick element was chosen to model the concrete elements except for haunch areas which used six-node isoparametric solid wedge elements. The material behavior of the concrete elements utilizes an orthotropic, smeared crack model, parallel to the principal strain directions, based on the rotating crack behavior. This concrete material model follows the method by Thorenfeldt et al. (1987) using the ultimate strength obtained from cylinder tests. The reinforcing steel was modeled as truss elements and assumes an elasto-plastic material property. For the loading areas and support regions, the same 8-node elements were used, but with linear elastic material properties and a high stiffness.

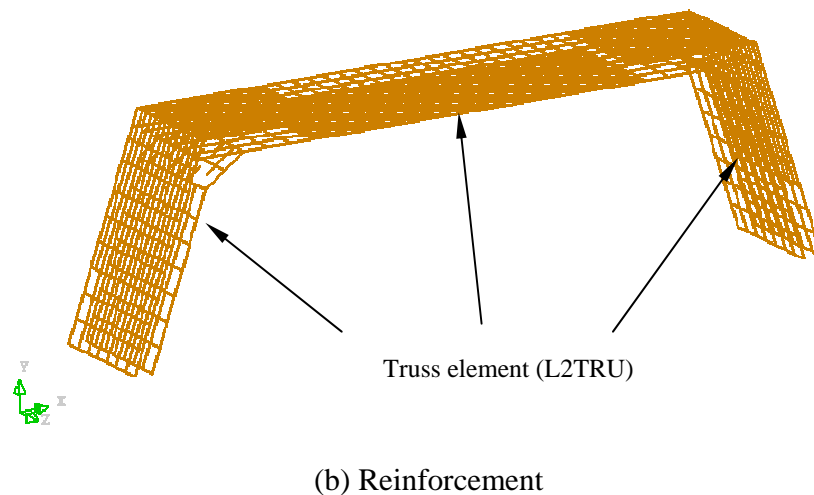
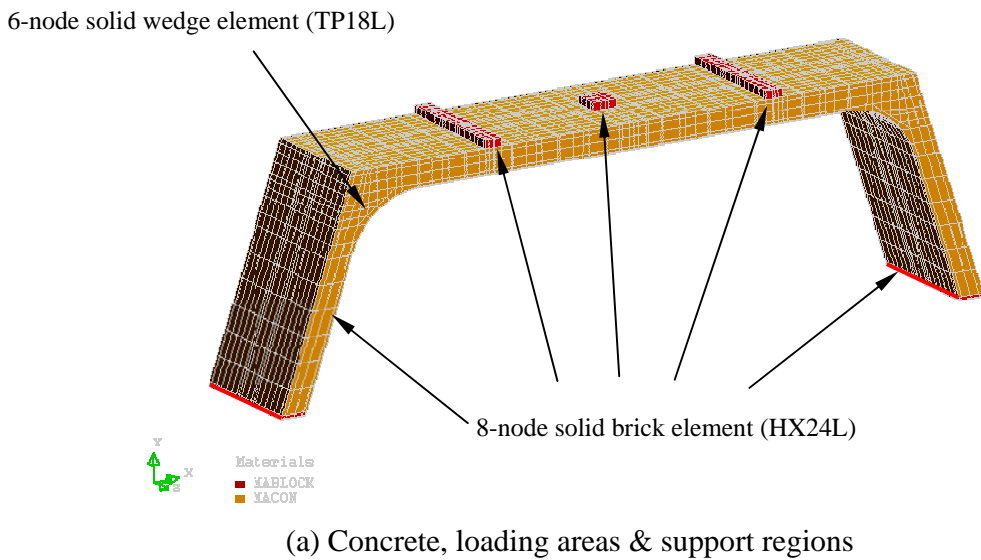
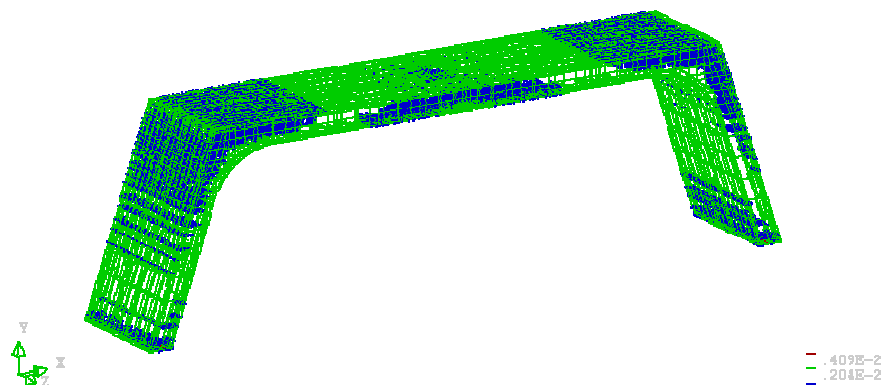


Figure 4.4. Finite Element Model

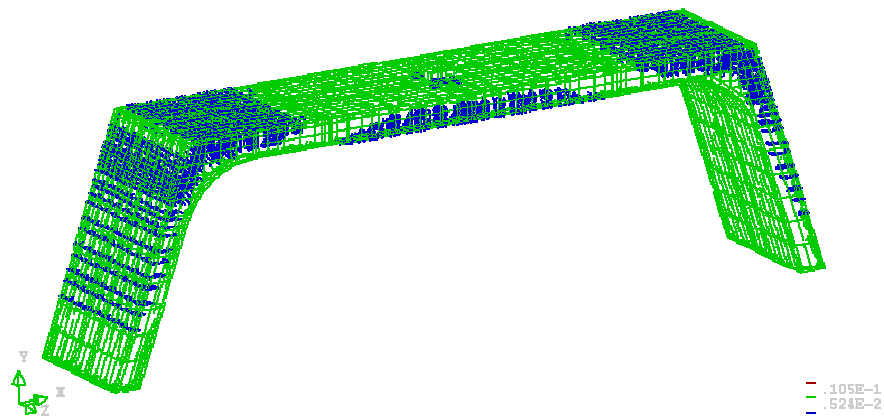
4.5. Results and Discussion

Analytical results such as overall behavior, failure modes and stress variations in steel and concrete are summarized and discussed for the second FE model. As mentioned above, there

was a significant difference in the failure mode between the experimental and analytical results of the first FE model. Crack patterns of the first FE model at the ultimate state are shown in Figure 4.5(a). Many cracks are shown on both the inside and outside surfaces of both legs. This type of crack behavior was not observed during any of the test load cases. The crack patterns from the second FE model are shown in Figure 4.5(b) and much more closely resemble the crack patterns observed during testing. Thus, it is clear that the first FE model was not suitable for comparison with the experimental results and the initial assumption of fixed boundary conditions was incorrect.



(a) First FE Model

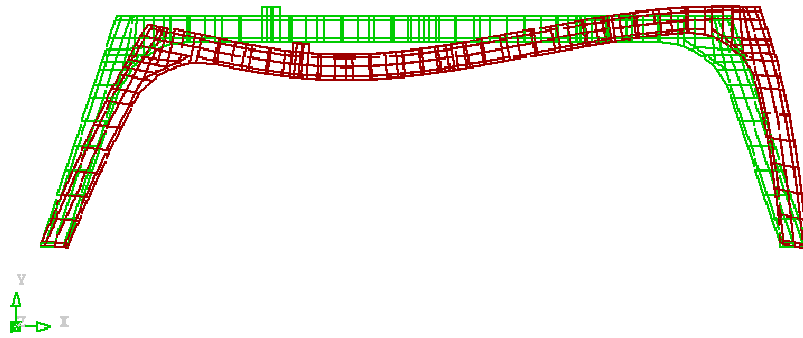


(b) Second FE model

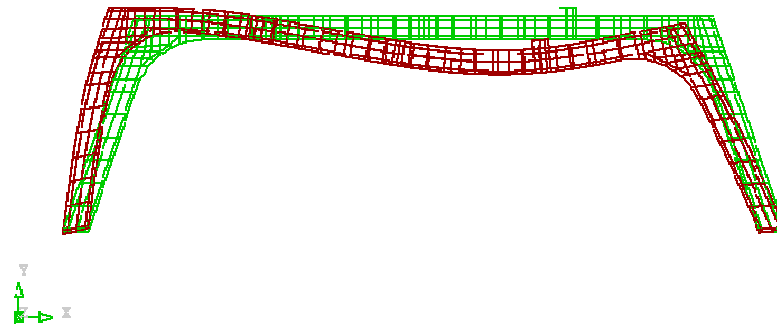
Figure 4.5. Crack Patterns at the Ultimate State

4.5.1. Load-Displacement Relation

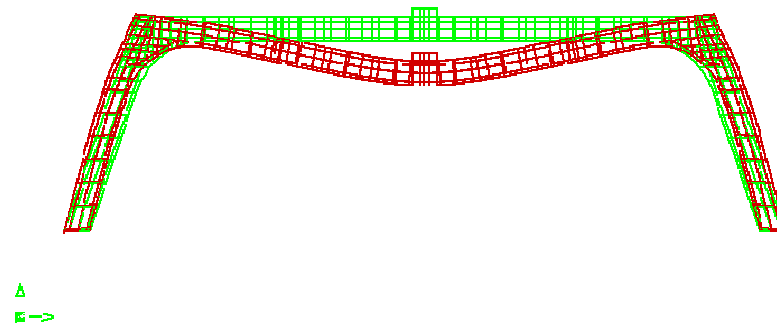
Deformed shapes at the ultimate state in each phase are illustrated in Figure 4.6. Load-displacement relationships are evaluated at the locations noted in Figure 4.7. Actual displacements for D1, D2 and D3 were taken from the bottom surface of slab while the figure indicates that these points are on the upper surface simply for the sake of visuals. Figure 4.8 shows the displacements of D1, D2 & D3 with respect to each phase.



(a) Phase I



(b) Phase II



(c) Phase III

Figure 4.6. Deformed Shapes in Each Phase

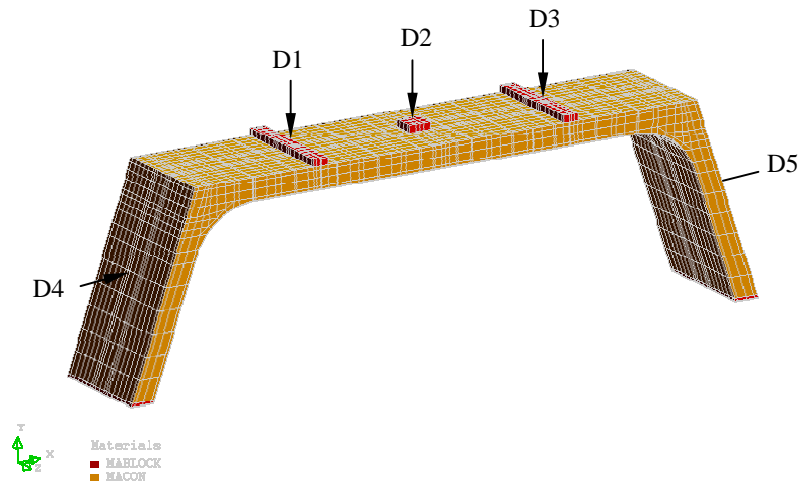
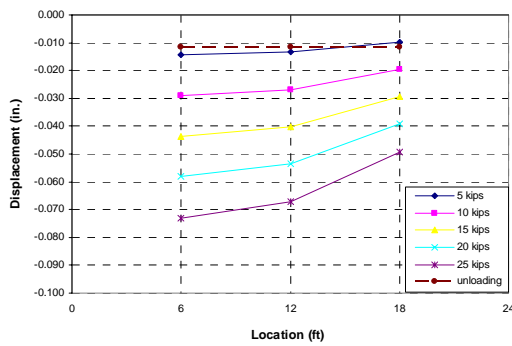
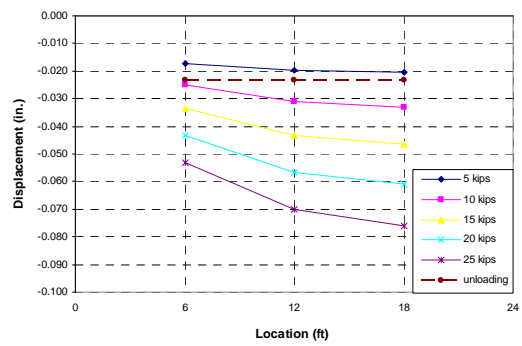


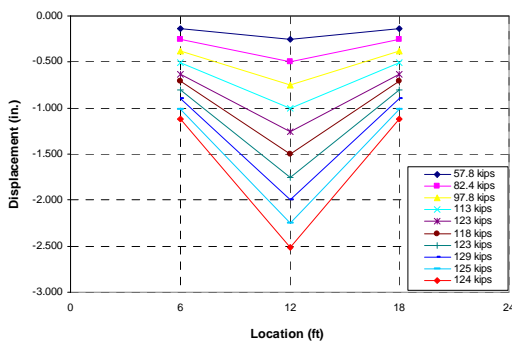
Figure 4.7. Measuring Points for Displacement



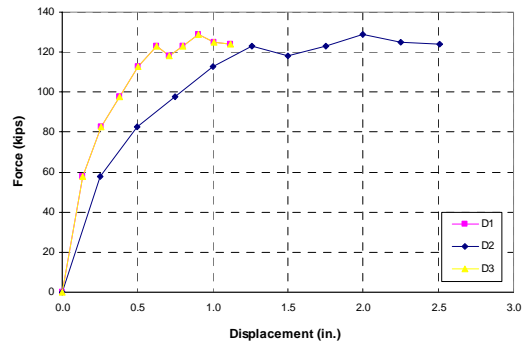
(a) Phase I



(b) Phase II



(c) Phase III along length



(d) Phase III at the points

Figure 4.8. Displacements at D1, D2 & D3

Displacements from the phase II analysis are larger than those of phase I due to plasticized regions caused by the cumulative loading effect of phase I, which can be clearly seen in Figure 4.8(a) and 4.8(b). Further, residual displacements are apparent after the unloading. Supplemental discussion of these residual displacements will be made in the section on stress variation. Displacements in phase III are very nearly symmetrical as shown Figure 28(c) and 28(d) without any affect from previous loading.

Displacements at points D4 and D5 are shown in Figure 4.9. The trends of these displacements are similar to those of the vertical displacements shown in Figure 4.8.

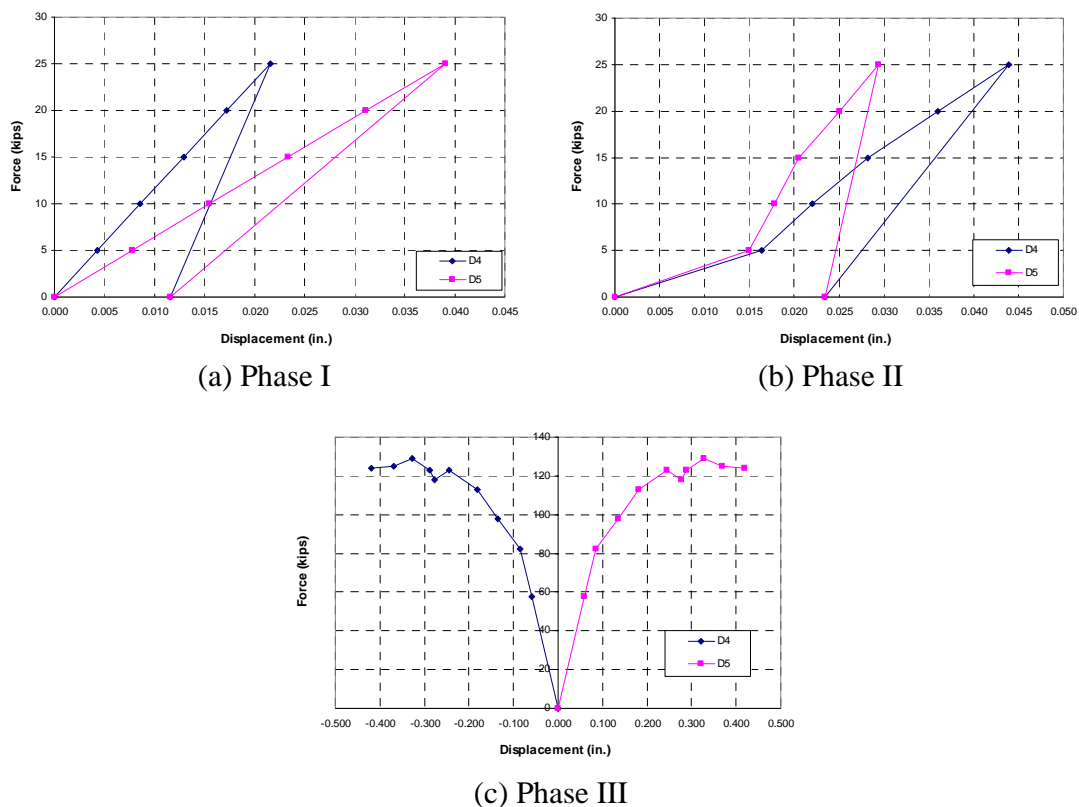


Figure 4.9. Displacements at the D4 & D5

The locations of reported displacements along the cross section at the mid point are shown in Figure 4.10. The displacements at these points for phase III are shown in Figure 4.11. As shown in the figure, there are no differences between those displacements. Thus, it can be concluded that there is no significant two-way slab action.

4.5.2. Crack patterns and Failure Modes

Figure 4.12 shows the crack patterns of phase I and II at the peak load of 25 kips. Pre-existing cracks caused by phase I loading are shown in Figure 4.12(b). In phase III, there were two peak points as shown in Figure 4.8(d). The first peak point was caused by yielding of the bottom reinforcement in the positive moment region. Beyond that, the top surface of the slab in the positive moment region began to crush with the simultaneous yielding of the top reinforcement

in the negative moment region. This failure mode can be observed from the crack patterns shown in Figure 4.13. The crack patterns at the first peak point are illustrated in Figure 4.13(a) and 4.13(b) while Figure 4.13(c) illustrates the second peak point.

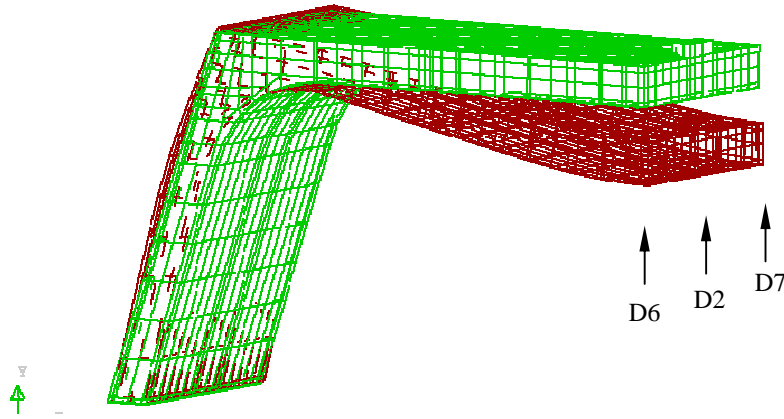


Figure 4.10. Measuring Points for Displacement

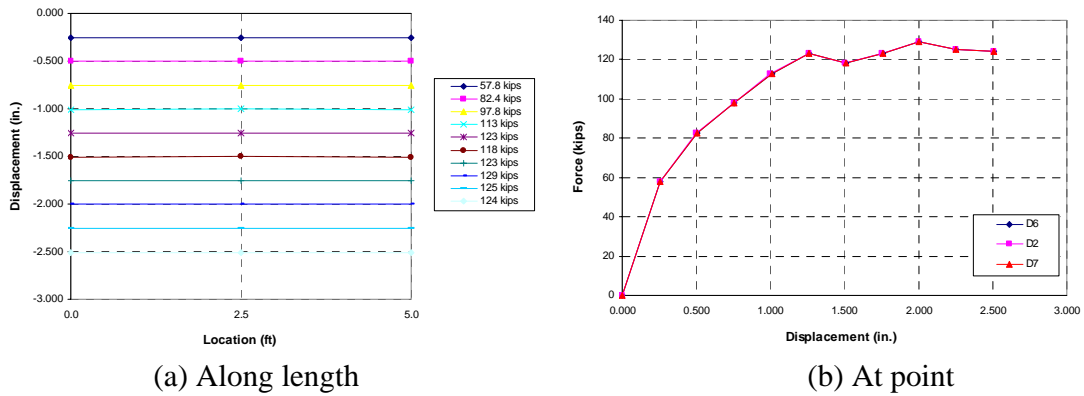


Figure 4.11. Displacements at D6, D2 & D7 for phase III

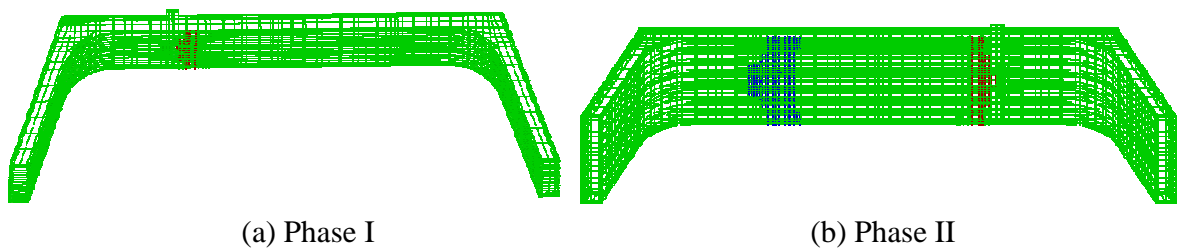
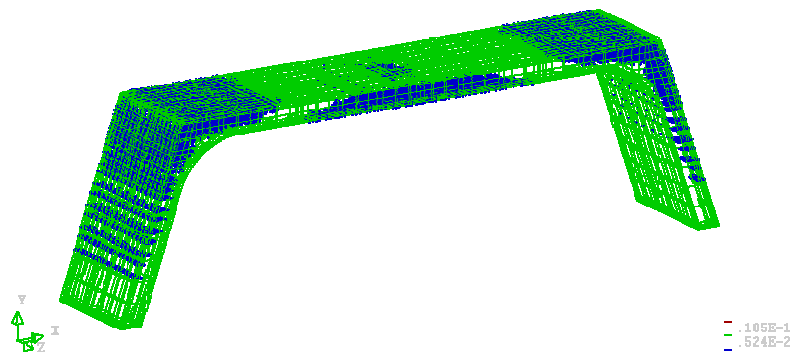


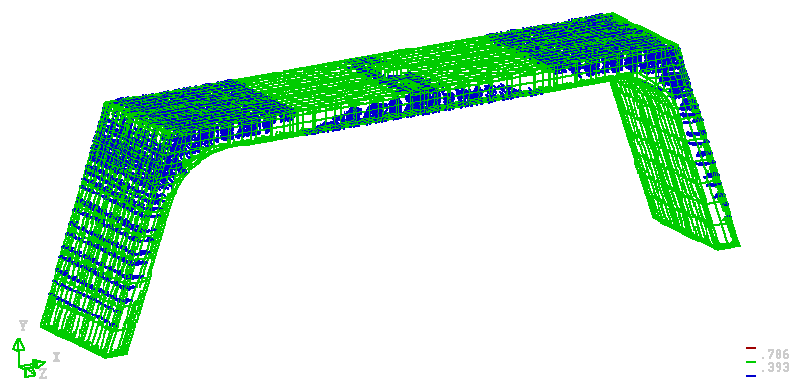
Figure 4.12. Crack Patterns of Phase I and II



(a) Upper view for the first peak point



(b) Lower view for the first peak point

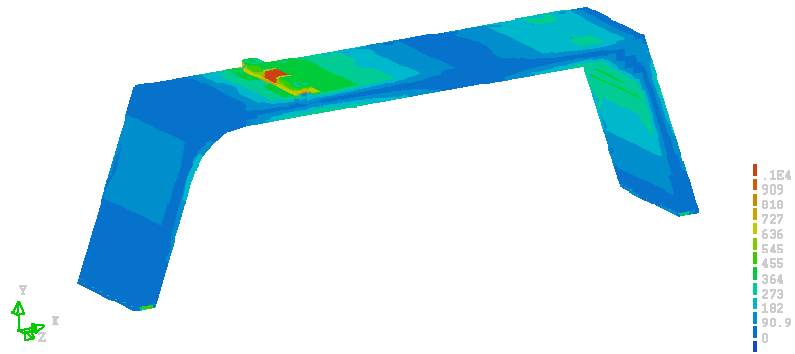


(c) Upper view for the second peak point

Figure 4.13. Crack Patterns of Phase III

4.5.3. Stress Variations on Concrete (Von Mises Stress)

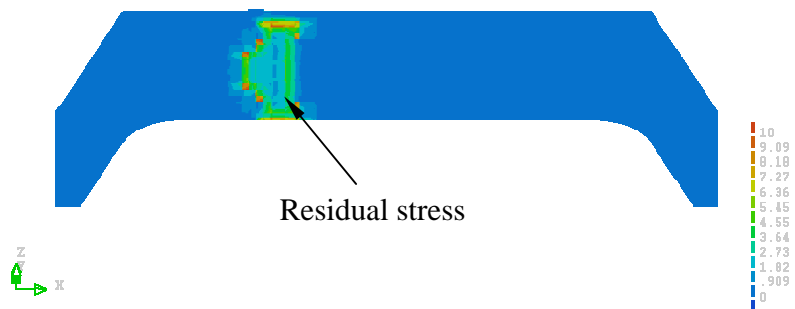
In order to investigate the severity of damage leading up to failure, a Von Mises stress contour was plotted on the concrete for each phase. These stress contours are illustrated in Figures 4.14 thru 4.16.



(a) Upper view at the peak loading state

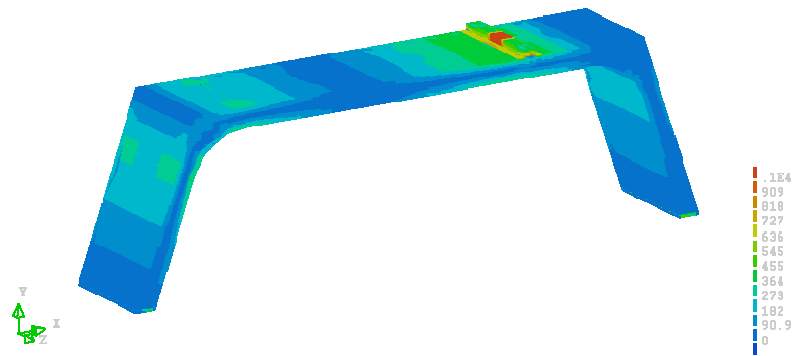


(b) Lower view at the peak loading state



(c) Lower view at the unloading state

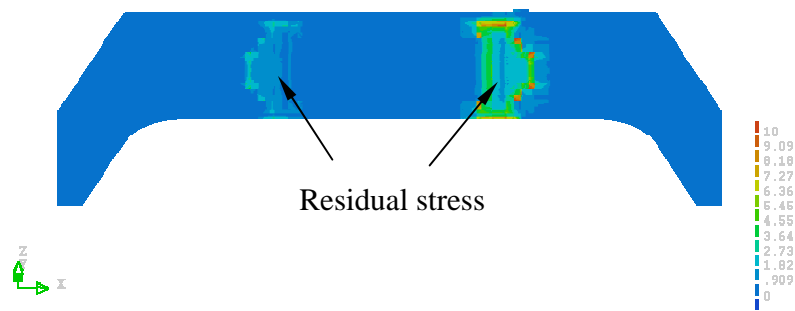
Figure 4.14. Von Mises Stress Contour for Phase I



(a) Upper view at the peak loading state

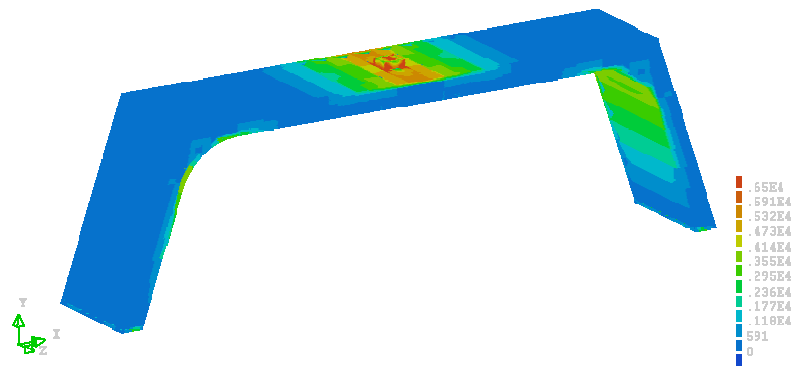


(b) Lower view at the peak loading state



(c) Lower view at the unloading state

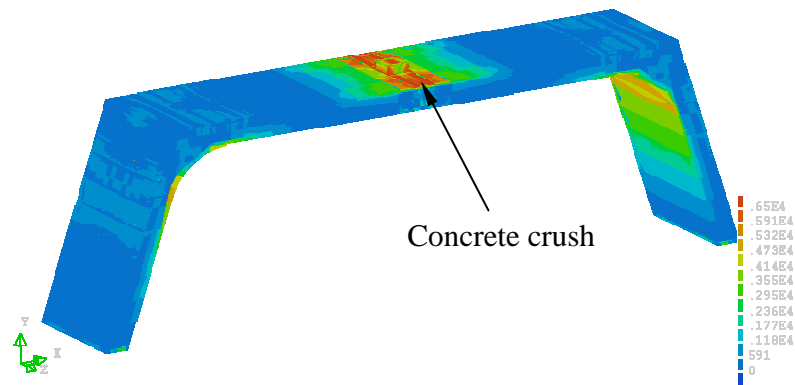
Figure 4.15. Von Mises Stress Contour for Phase II



(a) Upper view at the first peak loading state



(b) Lower view at the first peak loading state



(a) Upper view at the second peak loading state

Figure 4.16. Von Mises Stress Contour for Phase III

4.5.4. Stress Variations in Steel Reinforcement (Principal Stresses)

Principal stresses on all reinforcement are shown in Figures 4.17 through Figure 4.20. These stress variations supplement the failure modes described above.

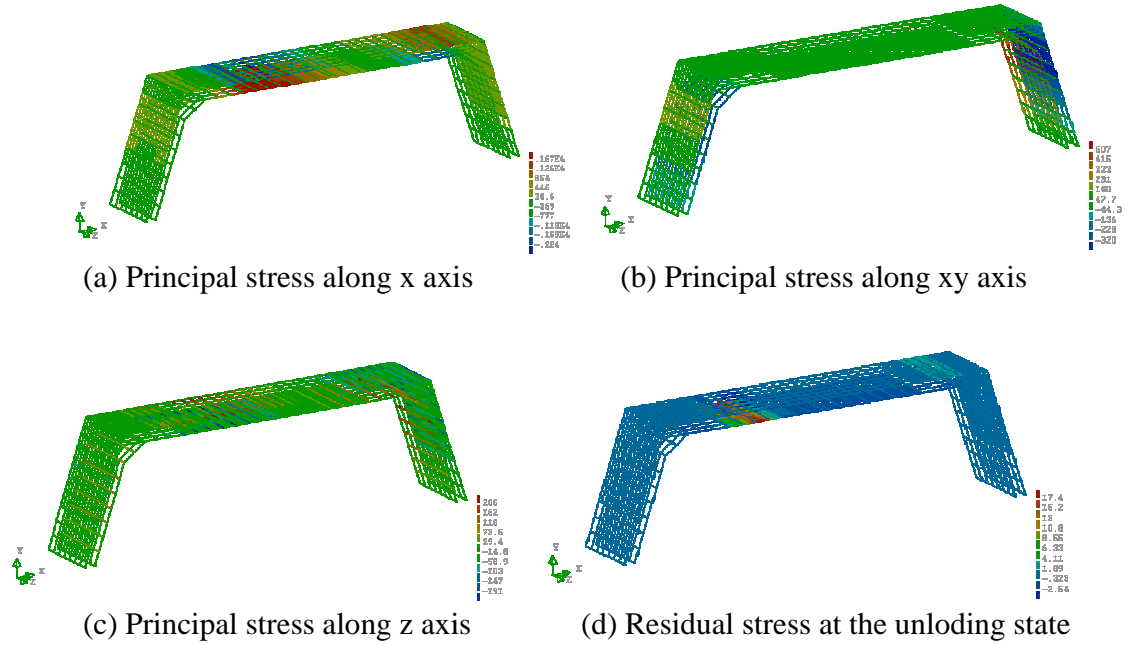


Figure 4.17. Principal Stress on Steel for Phase I

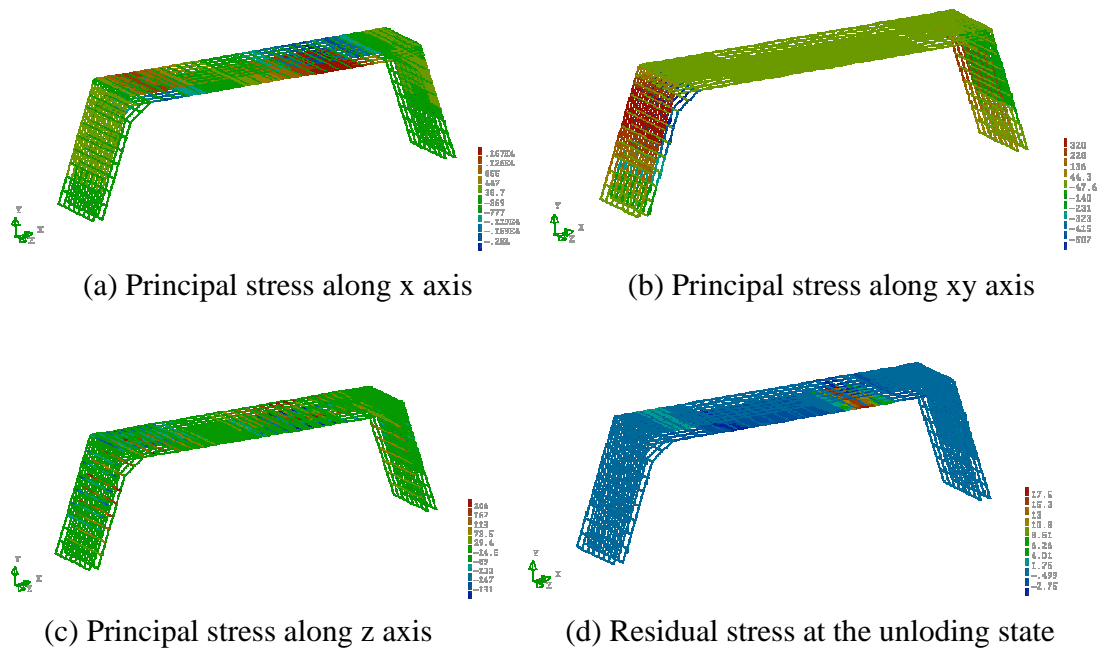


Figure 4.18. Principal Stress on Steel for Phase II

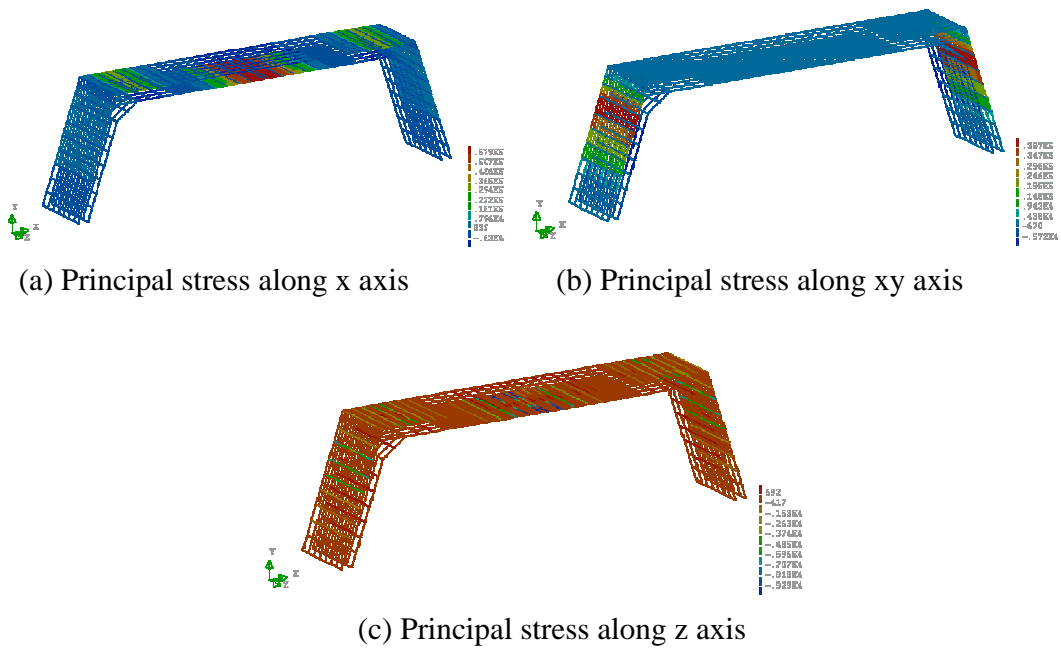


Figure 4.19. Principal Stress on Steel for Phase III (First Peak Loading State)

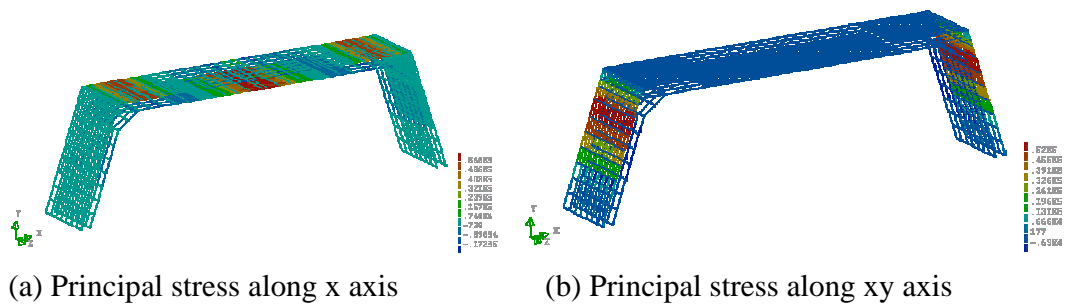


Figure 4.20. Principal Stress on Steel for Phase III (Second Peak Loading State)

5. CONCLUSIONS

A three-sided structure designed and constructed by Egyptian Concrete Co. was tested at the High-bay Structures Laboratory at the Missouri University of Science and Technology and the structural performance was evaluated based on experimental test results and finite element analysis, both of which have led to the following conclusions:

1. A prestressing strand was connected between the two inclined legs of the test specimen and prestressed to keep the legs from spreading or sliding during transportation, handling and installation. Once the test specimen was set in place, the prestressing force was released. The horizontal reaction force was measured at one side of the test specimen during the detensioning process. Measurements indicate that the entire prestressing force was transferred to a horizontal reaction force into the restraint blocks.
2. Load Cases 1 and 2 used a line load offset a distance of 6 ft from the mid-span and the test specimen was incrementally loaded up to 25 kips which was approximately the calculated flexural cracking load. At this load, the measured deformations appeared to be minimal and, as expected, the reinforcement did not yield.
3. The deflections at the loading point were slightly greater in Load Case 2 than in Load Case 1. This was due to specimen cracking that occurred during Load Case 1 which produced a slightly more flexible structure when it was subjected to Load Case 2.
4. The failure of the test specimen during Load Case 3 occurred in the following order: (1) yielding of the tensile reinforcement at the mid-span of the slab due to the positive moment, (2) yielding of the tensile reinforcement in the upper portion of the legs near the haunches due to the negative moment, (3) yielding of the tensile reinforcement in the slab near the haunches due to the negative moment, and (4) crushing of concrete at mid-span.
5. The load that produced yielding of the tensile reinforcement at mid-span of the slab was approximately 70 kips while the failure load at crushing of concrete was approximately 107 kips.
6. It was observed from the strain variation in the reinforcement near the cutoff points that the point of inflection moved toward the cutoff points after yielding of the reinforcement at the mid-span of the slab.
7. It could be said that based on the strains measured from the LVDTs attached to the legs that the reinforcement and concrete below the mid-height of the legs would not yield or reach its ultimate compressive strain.
8. The horizontal reaction forces appeared to be about 32% of the total applied load based on three Load Cases.
9. At the service load (50 kips), which was estimated as about 70% of the load at yield of the reinforcement at the mid-span of the slab, 70 kips, the measured maximum deflection was less than the maximum permissible computed deflections specified in Section 9.5.2.6 of ACI 318-05 but greater than the requirement specified in Article 2.5.2.6.2 in the AASHTO LRFD specifications.
10. The concentrated load was effectively distributed across the entire transverse direction of the slab and did not exhibit two-way slab actions.
11. The FEM results showed stiffer behavior than the experimental results, and the predicted failure load of 129 kips was just 20% higher than the test result of 107 kips. The stiffer behavior of FEM results could be due to the fact that in the FEM analysis, the horizontal

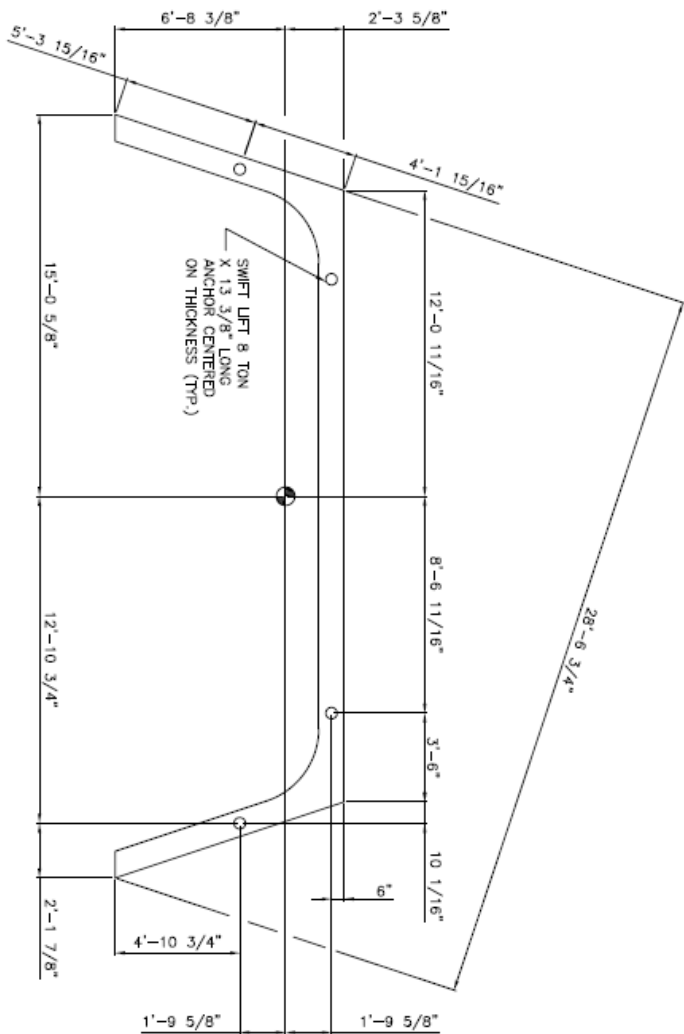
displacement of the bottoms of the legs was perfectly restrained while during testing, the bottoms of the legs moved outward slightly in horizontal direction.

6. REFERENCES

- AASHTO (2003), AASHTO LRFD Bridge Design Specifications with 2003 Interim Revisions, American Association of State Highway and Transportation Officials, Washington, DC.
- ACI (2005), ACI 318-05 Building Code Requirements for Structural Concrete (318-05) and Commentary (318-05R), American Concrete Institute, Farmington Hills, MI.
- American Concrete Industries,
www.americanconcrete.com, Last Accessed July 2008.
- ASCE, (2001) ASCE 2001 Report Card,
<http://www.asce.org/reportcard/index.cfm?reaction=full&page=2>, Last Accessed July 2008
- ASCE, (2005) ASCE 2005 Report Card <http://www.asce.org/reportcard/2005/index2005.cfm>, Last Accessed July 2008
- ASTM C1433 - 08 Standard Specification for Precast Reinforced Concrete Monolithic Box Sections for Culverts, Storm Drains, and Sewers, ASTM International, West Conshohocken, PA.
- Con/Span Bridge ® Bridge Systems,
<http://www.con-span.com/con-span/main.html>, Last Accessed July 2008.
- Thorenfeldt, E., Tomaszewics, A., and Jensen, J. J. (1987), “ Mechanical Properties of High Strength Concrete and Applications in Design,” Third International Conference of Fracture Mechanics of Concrete Structures, D-Freiburg, Aedificatio Publication, pp. 1937-1948.

APPEINDIX A. SPECIMEN DETAILS

The following engineering drawings and details for the test specimen were provided by Egyptian Concrete Company, Inc.



REVISIONS

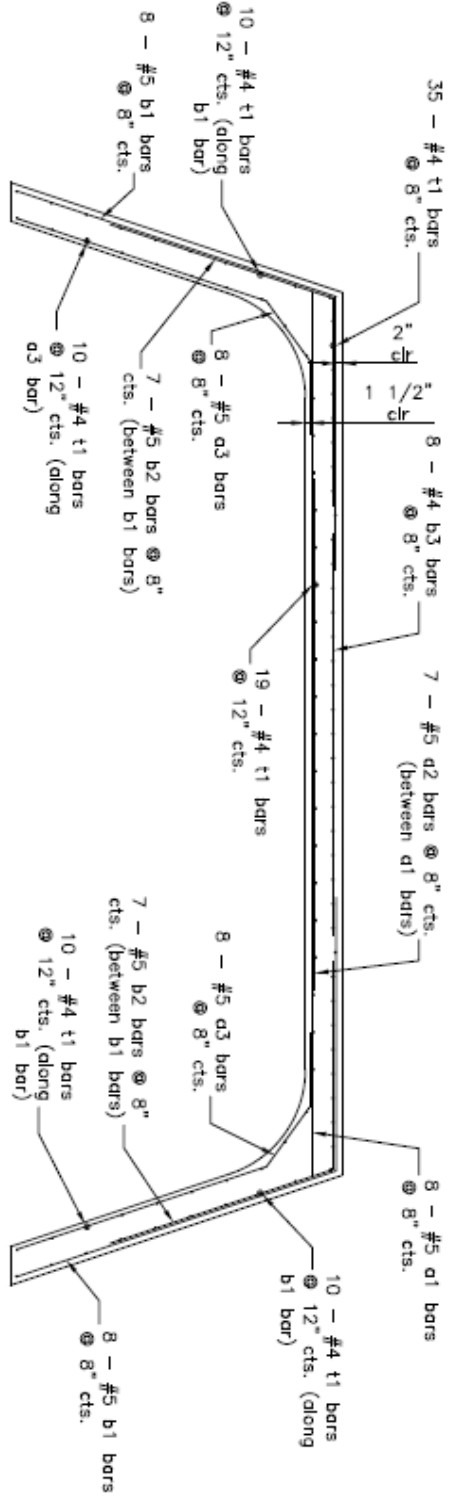
1	
2	
3	
4	
5	
6	
7	
8	



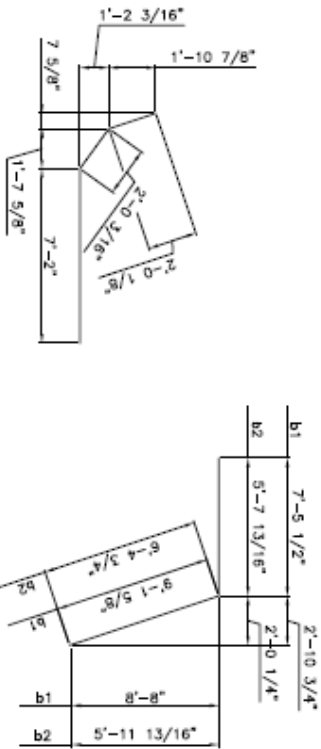
STRONGhold
STRONGHOLD TEST SECTION
CENTER OF GRAVITY AND LIFT POINTS

EGYPTIAN CONCRETE CO.
POST OFFICE BOX 488
SALEM, IL 62881
PHONE: (618) 548-1190
FAX: (618) 548-1294

SHEET
1
OF 2



TEST SECTION — REINFORCEMENT




BAR	SIZE	QUANTITY	LENGTH	SHAPE
a1	#5	8	24'-1"	—
a2	#5	7	14'-0"	—
a3	#5	16	11'-2"	—
b1	#5	16	16'-7"	—
b2	#5	14	12'-2"	—
b3	#4	8	11'-0"	—
t1	#4	94	4'-9"	—

BARs b1 AND b2

REVISIONS

NO.	DESCRIPTION	DATE	BY

DESIGNED BY:  STRONGHOLD TEST SECTION
 CHECKED BY: _____
 REINFORCEMENT DETAILS: _____

EGYPTIAN CONCRETE CO.
 POST OFFICE BOX 488
 SALEM, IL 62861
 PHONE: (618) 548-1190
 FAX: (618) 548-1294

APPENDIX B. TENSILE TEST RESULTS OF REINFORCING BARS

Three samples of #4 and #5 reinforcing bars were tested in the Materials Laboratory at Missouri S and T and the results are presented in this appendix.

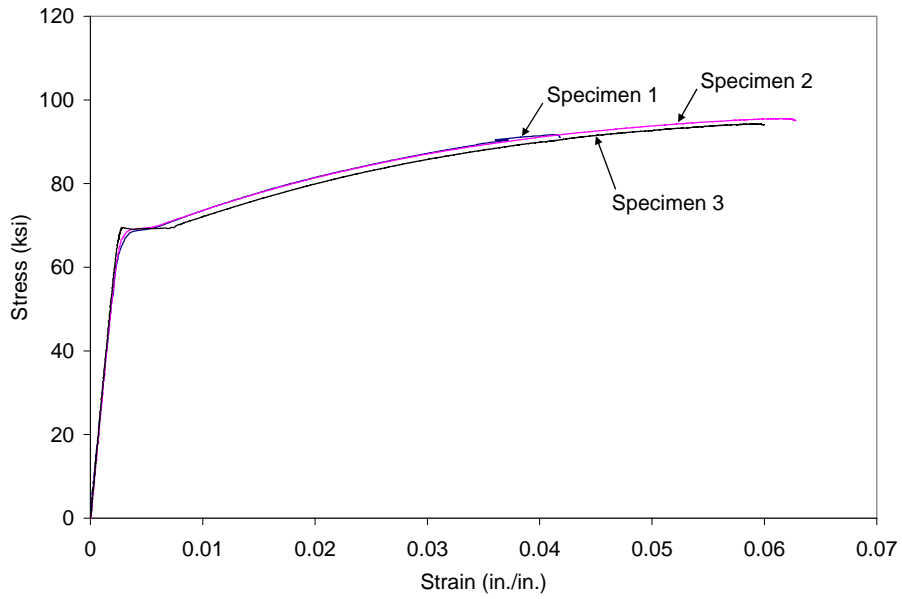


Figure B.1 Tensile Test Results of #4 Rebars

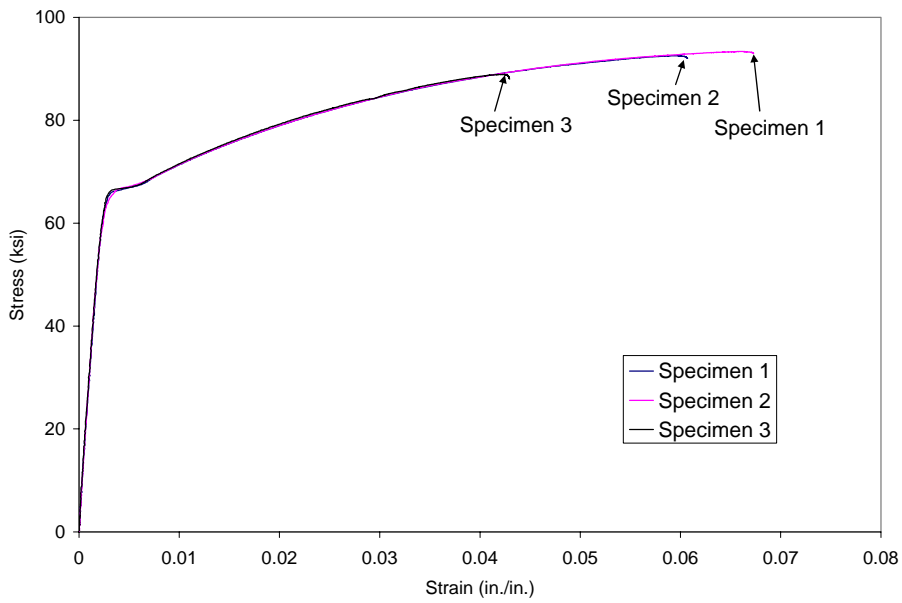


Figure B.2 Tensile Test Results of #5 Rebars

Table B.1 Tensile Test Results of #4 Reinforcing Bars

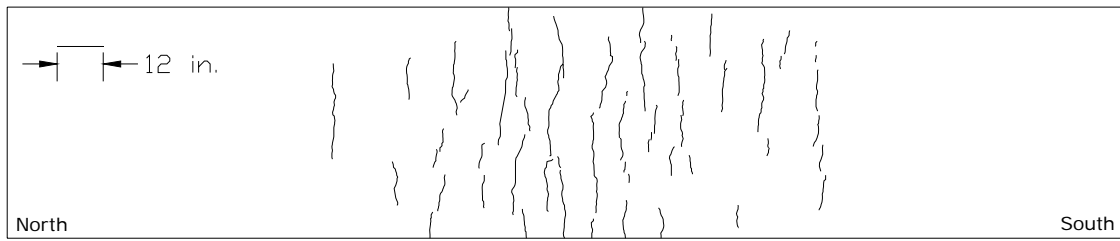
Specimen	Yield Strength, f_y (ksi)	Ultimate Strength, f_u (ksi)
1	69.0	91.7
2	69.2	95.1
3	69.0	94.0
Average	69.1	93.6

Table B.2 Tensile Test Results of #5 Reinforcing Bars

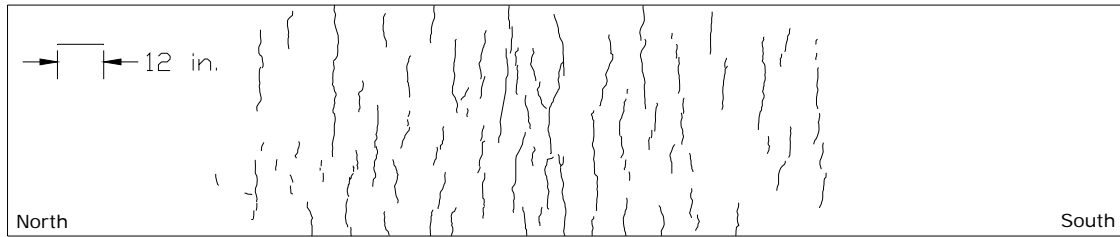
Specimen	Yield Strength, f_y (ksi)	Ultimate Strength, f_u (ksi)
1	65.9	92.8
2	66.7	93.1
3	65.9	88.8
Average	66.2	91.6

APPEINDIX C. CRACK PATTERNS

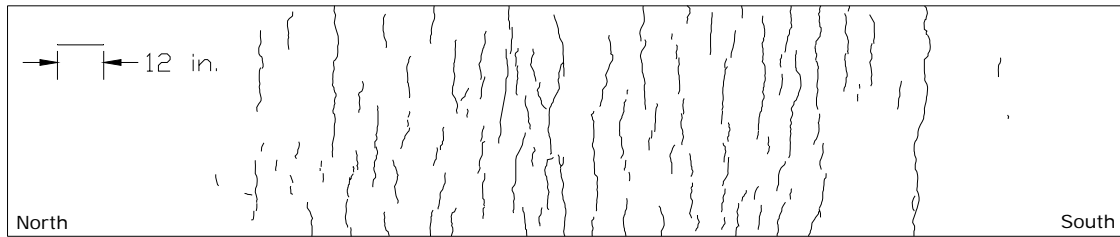
Cracks were marked before and during the tests and the crack patterns were drawn based on the marked cracks. The following figures show the crack patterns of the test specimen after each Load Case.



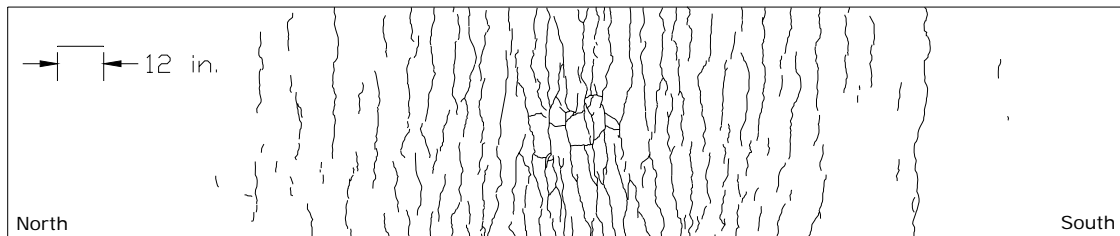
(a) Dry Shrinkage



(b) D-S + Load Case 1

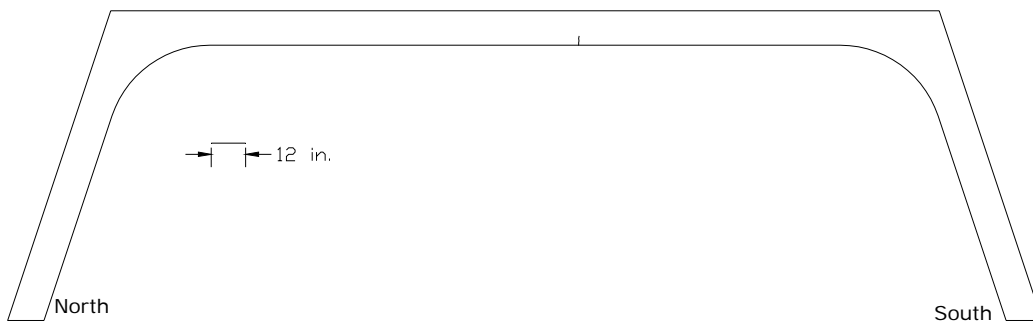


(c) D-S + Load Case 1 + Load Case 2

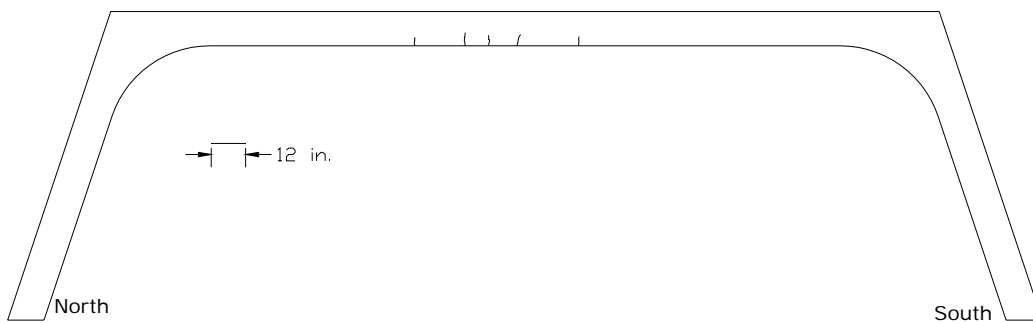


(d) D-S + Load Case 1 + Load Case 2 + Load Case 3

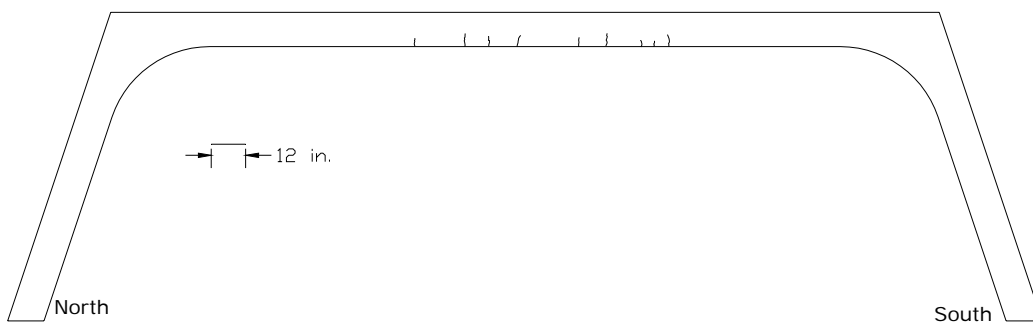
Figure C.1. Crack Patterns of Bottom Side of the Slab



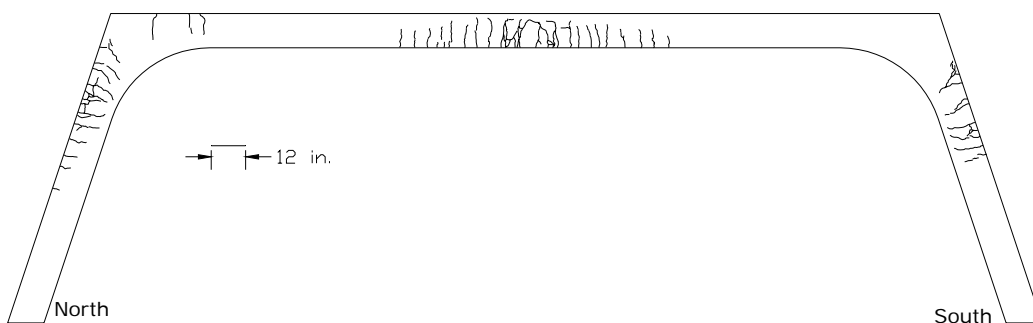
(a) Dry Shrinkage



(b) D-S + Load Case 1



(c) D-S + Load Case 1 + Load Case 2

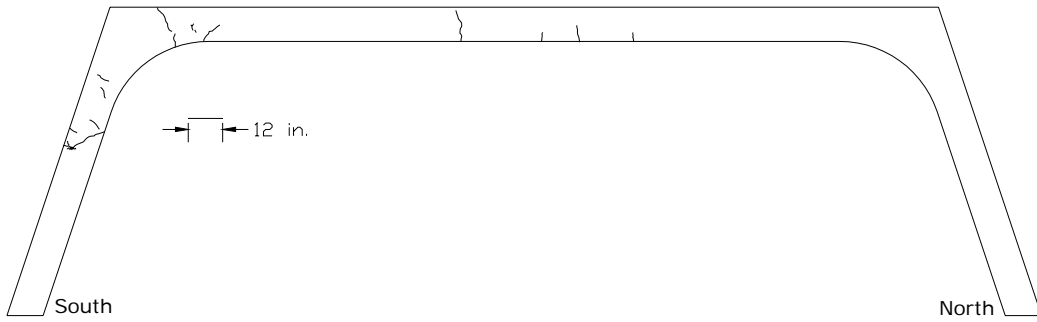


(d) D-S + Load Case 1 + Load Case 2 + Load Case 3

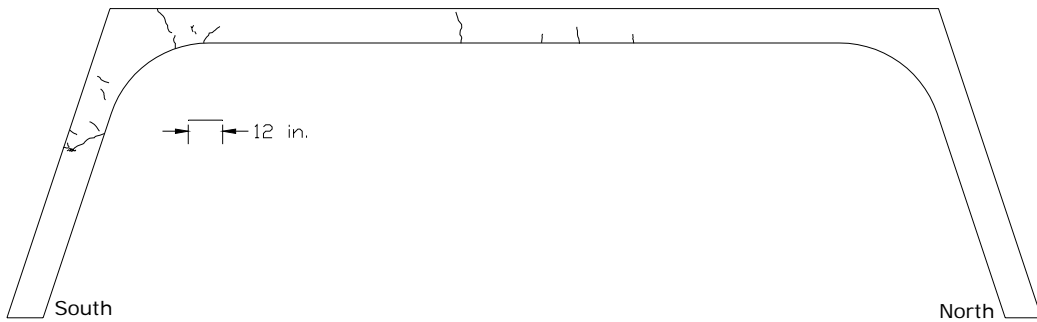
Figure C.2. Crack Patterns for West Side



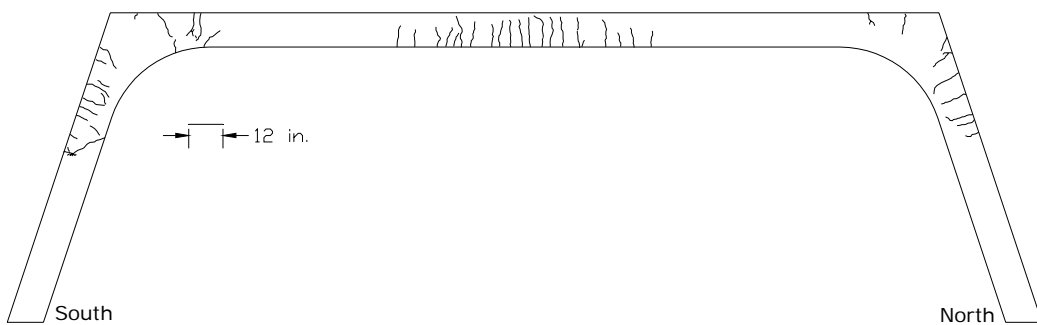
(a) Dry Shrinkage



(b) D-S + Load Case 1

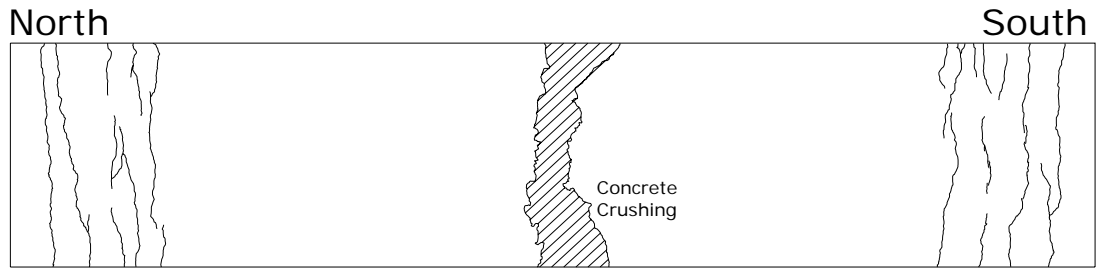


(c) D-S + Load Case 1 + Load Case 2



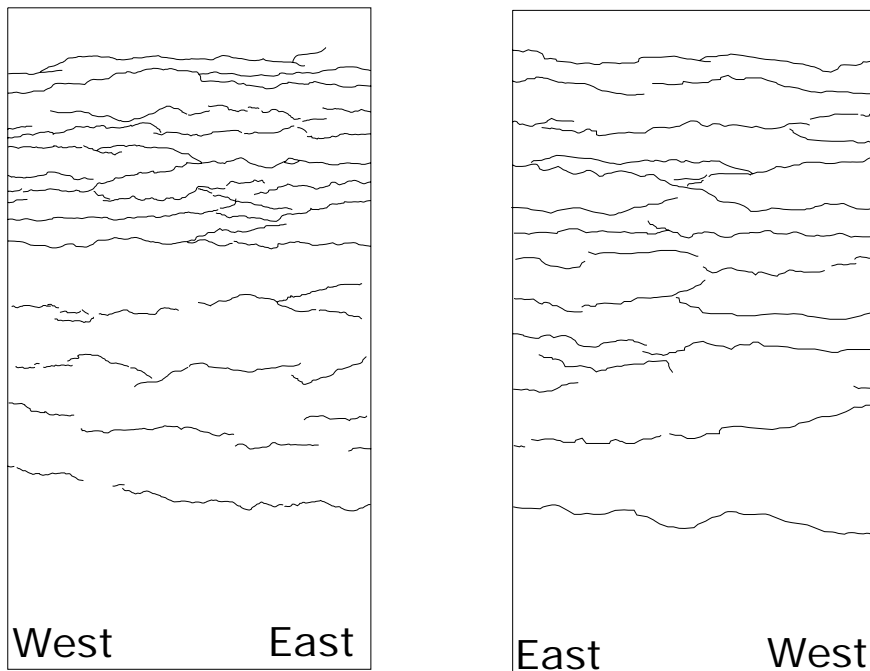
(c) D-S + Load Case 1 + Load Case 2 + Load Case 3

Figure C.3. Crack Patterns for East Side



Note: All cracks in this figure were developed due to Load Case 3. No cracks due to dry-shrinkage, Load Cases 1 and 2 were observed.

Figure C.4. Crack Patterns for the Top Side of the Slab



(a) South Leg

(b) North Leg

Note: All cracks in this figure were developed due to Load Case 3. No cracks due to dry-shrinkage, Load Cases 1 and 2 were observed.

Figure C.5. Crack Patterns for the Legs

APPENDIX D. TEST RESULTS OF LOAD CASE 1

Readings from all kinds of instrumentation are presented in this appendix, including strain gages in the reinforcement, LVDTs and load cells. Most of the graphs shown in this appendix are discussed in the main body of this report, except for some readings from strain gages.

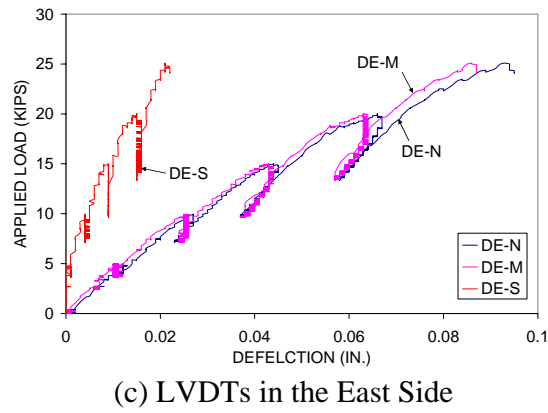
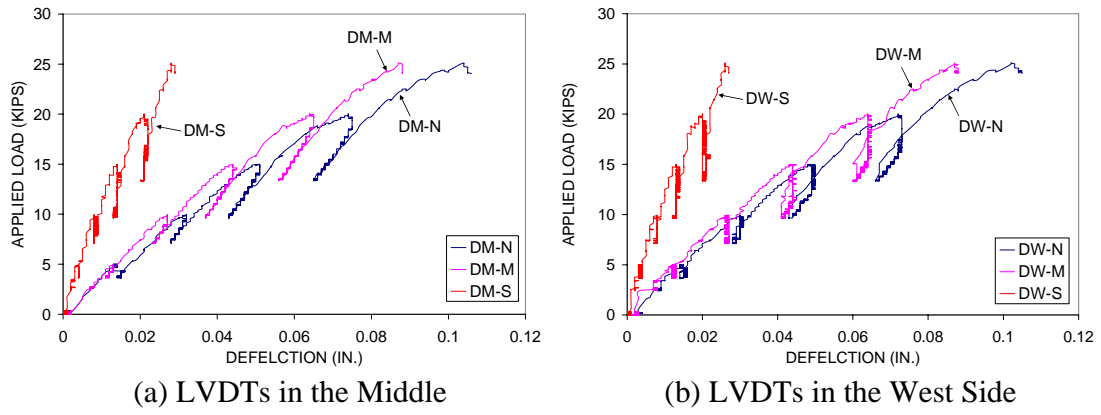


Figure D.1 Deflections in the Slabs

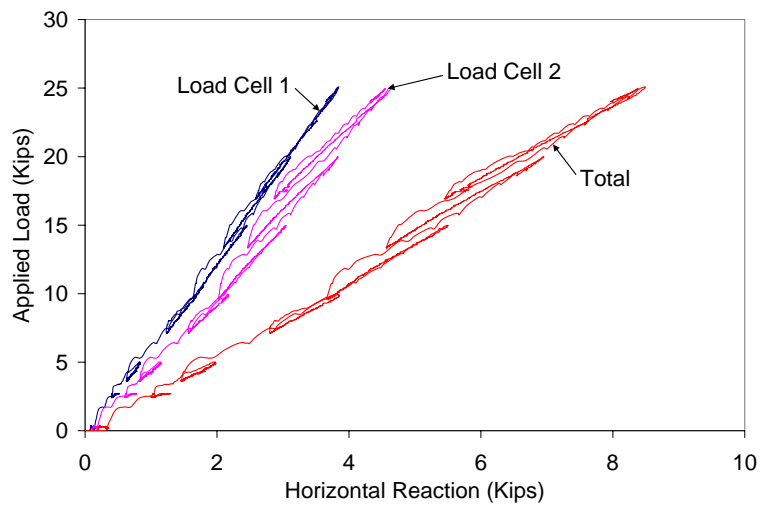


Figure D.2 Horizontal Reaction Forces

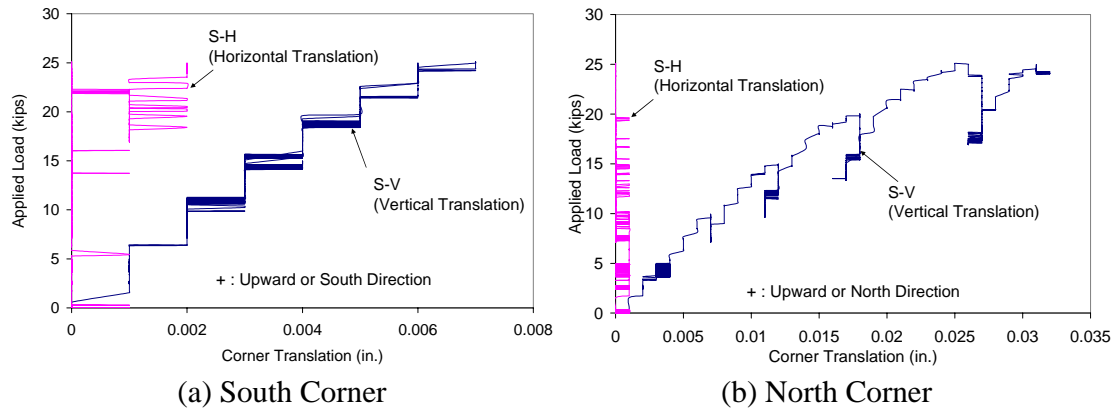
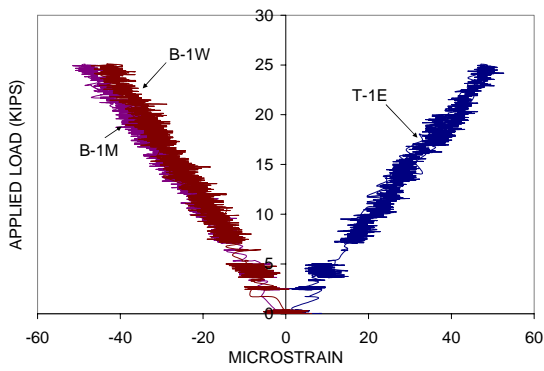
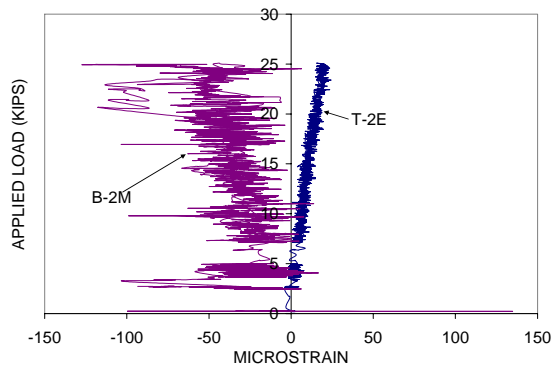


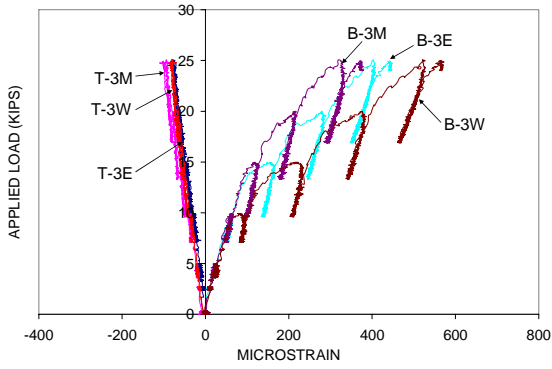
Figure D.3 Corner Translation



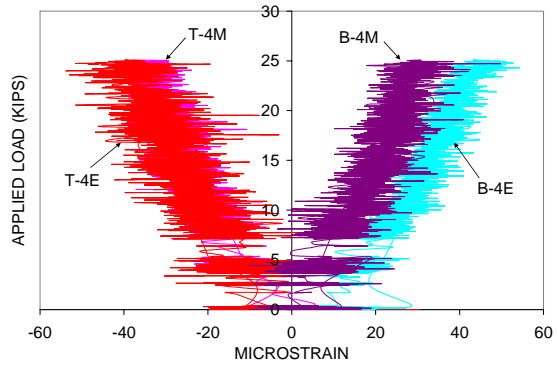
(a) T-1 and B-1 Series



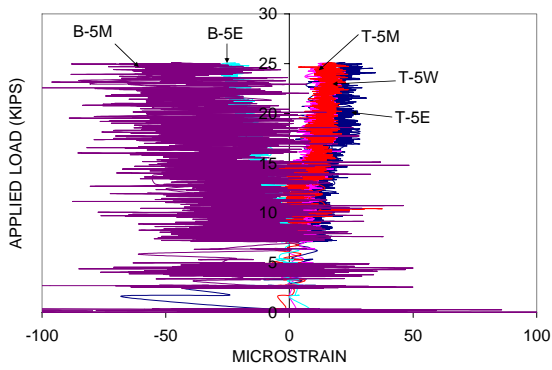
(b) T-2 and B-2 Series



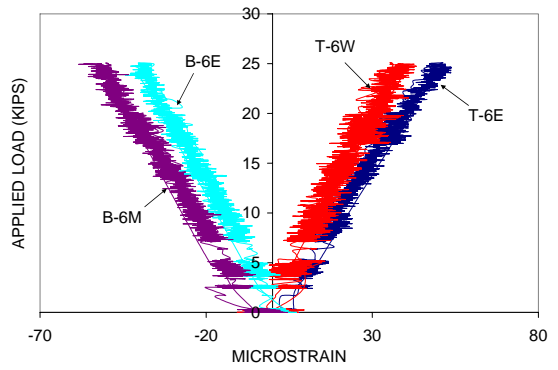
(c) T-3 and B-3 Series



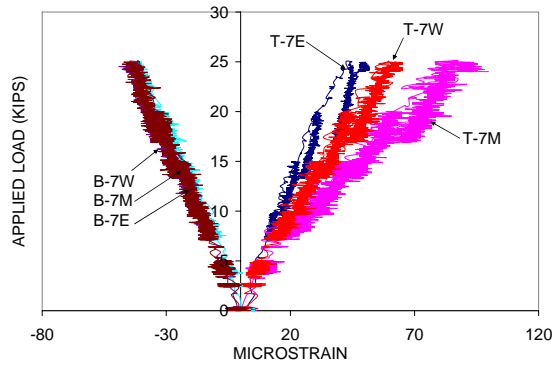
(d) T-4 and B-4 Series



(e) T-5 and B-5 Series



(f) T-6 and B-6 Series

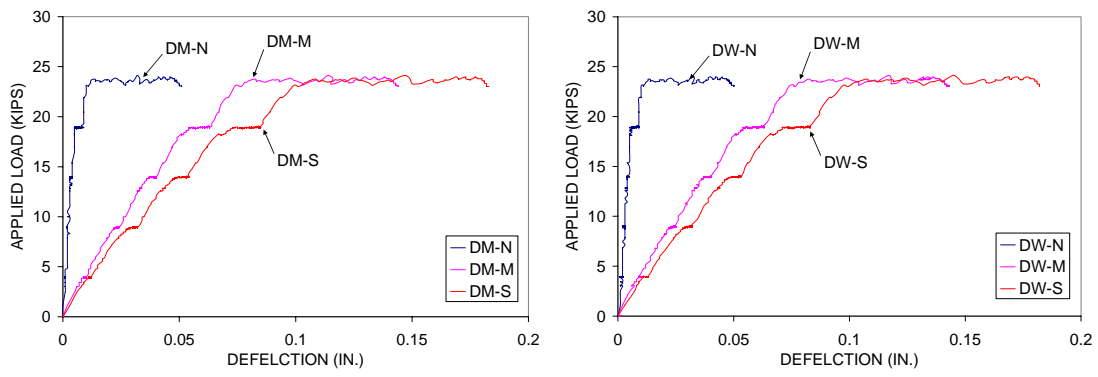


(g) T-7 and B-7 Series

Figure D.4 Strain of Reinforcement Measured from Strain Gages

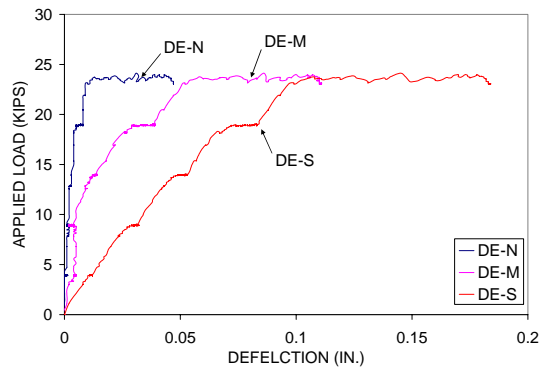
APPENDIX E. TEST RESULTS OF LOAD CASE 2

Readings from all kinds of instrumentation are presented in this appendix, including strain gages in the reinforcement, LVDTs and load cells. Most of the graphs shown in this appendix are discussed in the main body of this report as necessary, except for some readings from strain gages.



(a) LVDTs in the Middle

(b) LVDTs in the West Side



(c) LVDTs in the East Side

Figure E.1 Deflections in the Slabs

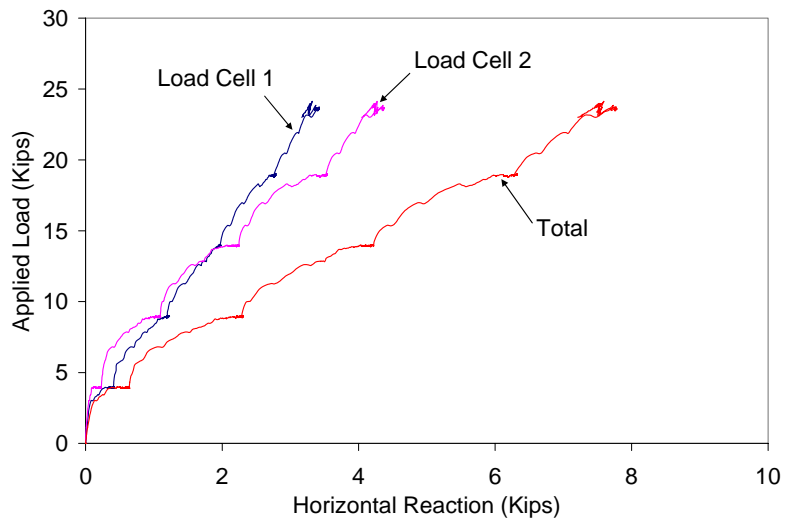


Figure E.2 Horizontal Reaction Forces

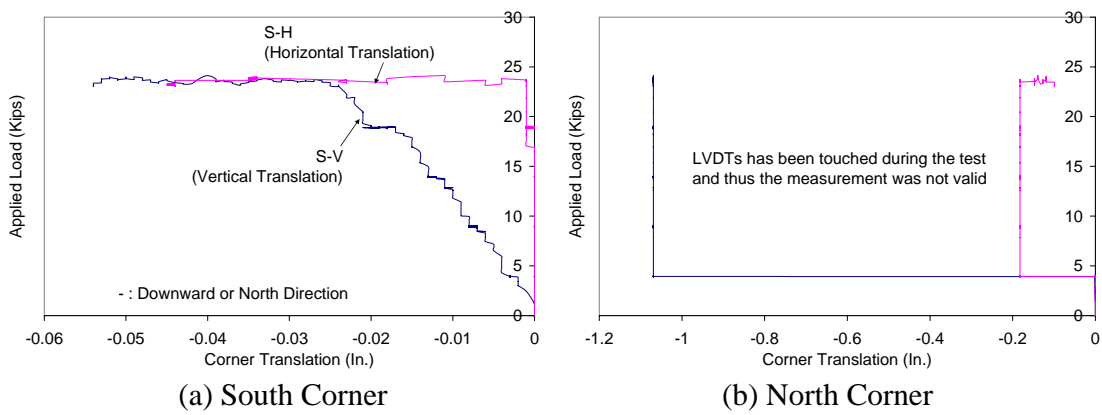
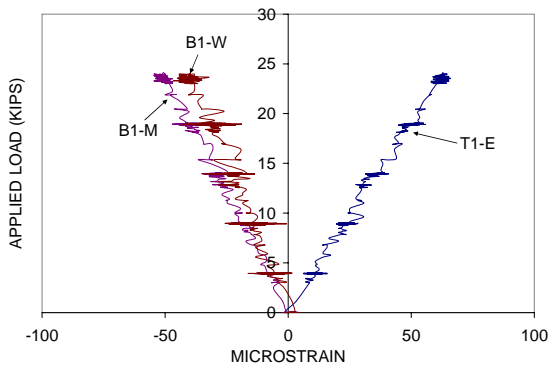
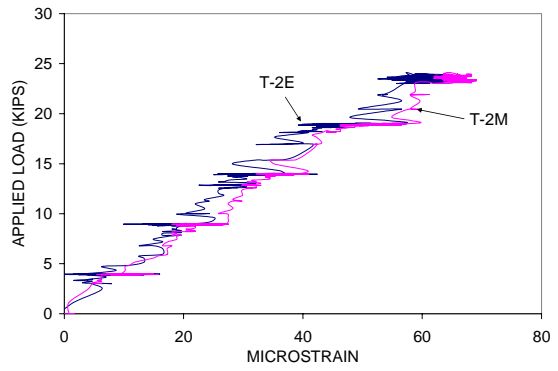


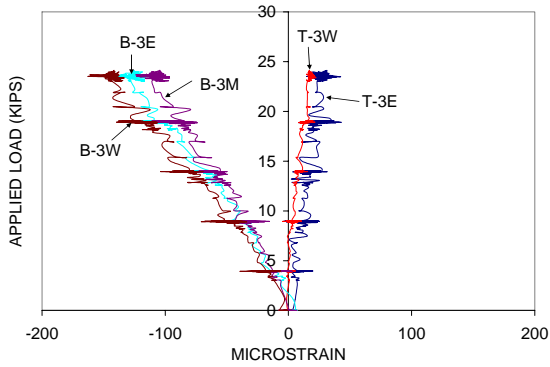
Figure E.3 Corner Translation



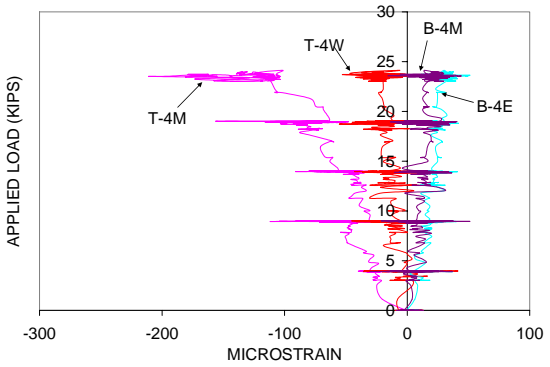
(a) T-1 and B1 Series



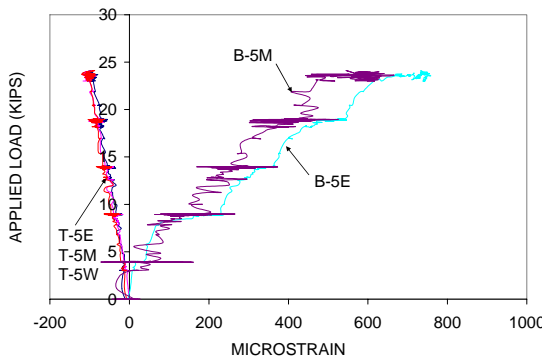
(b) T-2 and B-2 Series



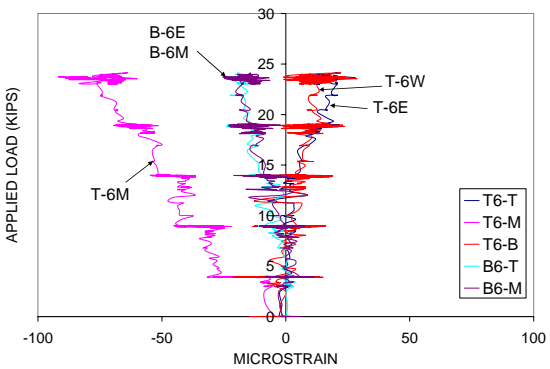
(c) T-3 and B-3 Series



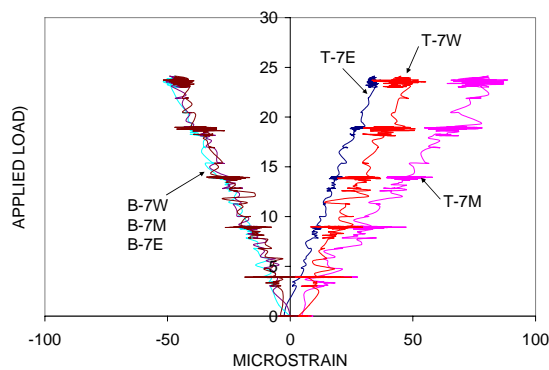
(d) T-4 and B-4 Series



(e) T-5 and B-5 Series



(f) T-6 and B-6 Series

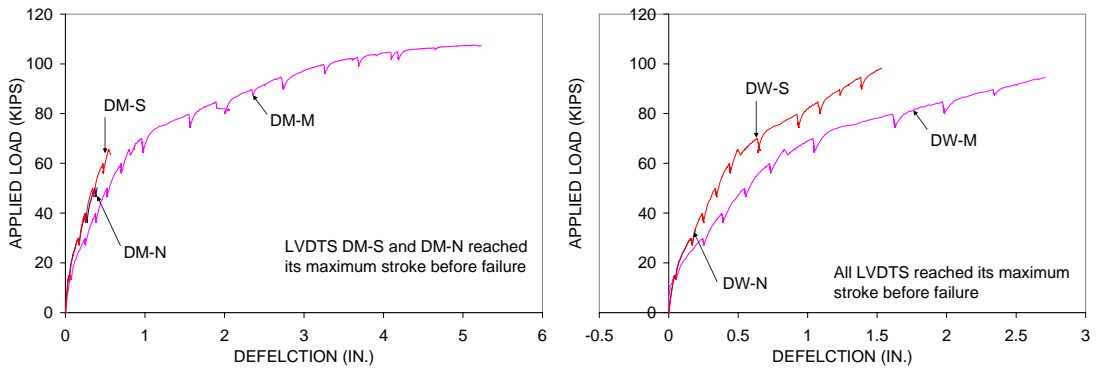


(g) T-7 and B-7 Series

Figure E.4 Strain of Reinforcement Measured from Strain Gages

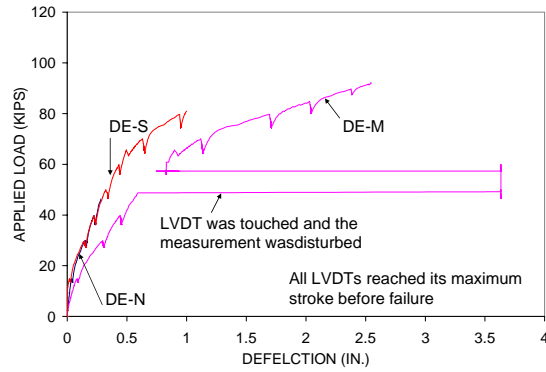
APPENDIX F. TEST RESULTS OF LOAD CASE 3

Readings from all kinds of instrumentation are presented in this appendix, including strain gages in the reinforcement, LVDTs and load cells. Most of the graphs shown in this appendix are discussed in the main body of this report, except for some readings from strain gages.



(a) LVDTs in the Middle

(b) LVDTs in the West Side



(c) LVDTs in the East Side

Figure F.1 Deflections in the Slabs

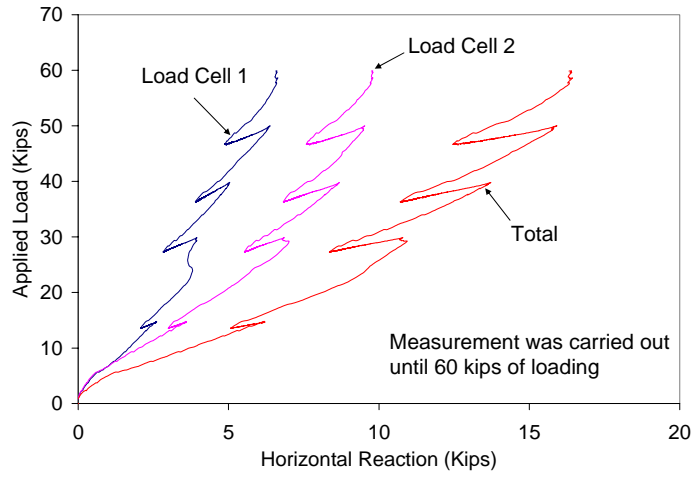


Figure F.2 Horizontal Reaction Forces

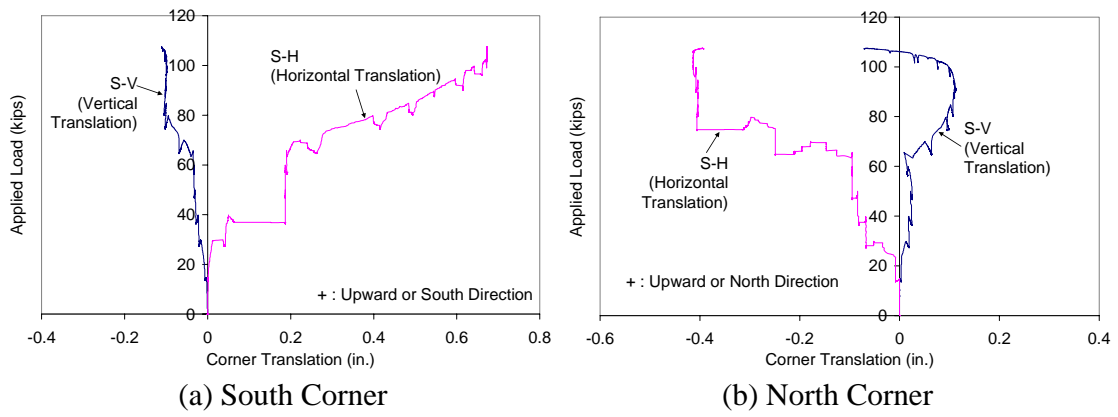
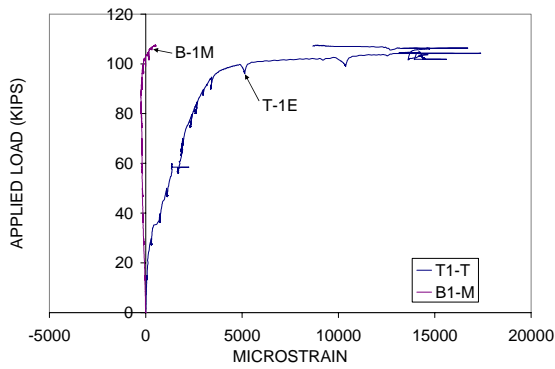
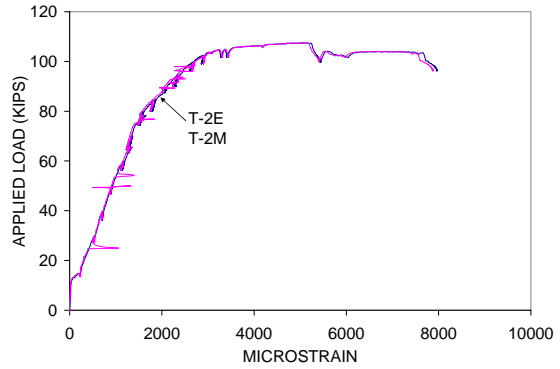


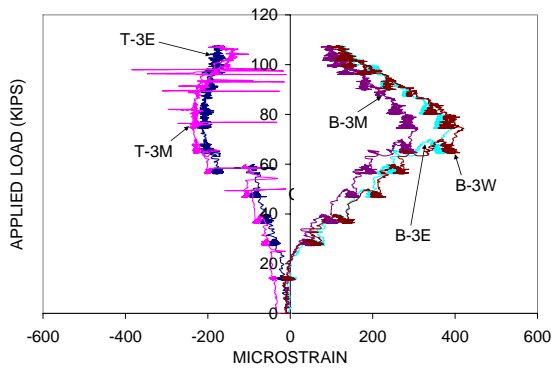
Figure F.3 Corner Translation



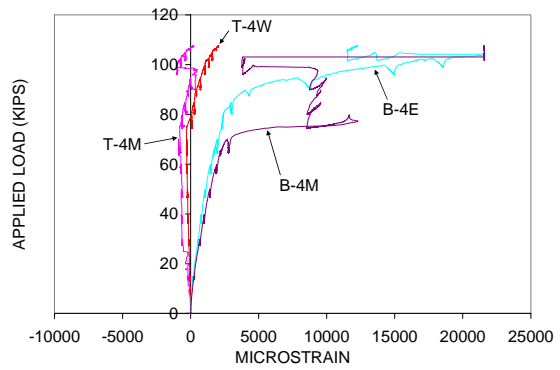
(a) T-1 and B1 Series



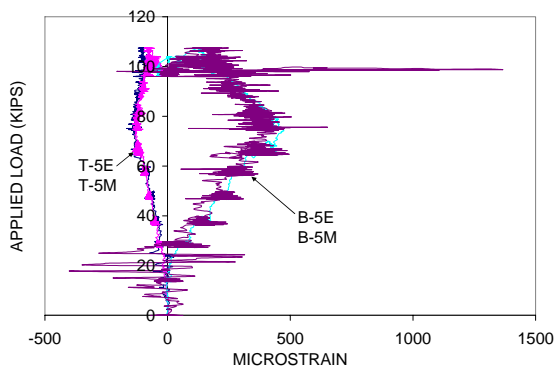
(b) T-2 and B-2 Series



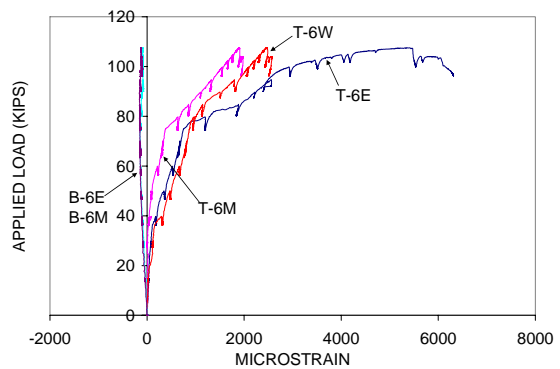
(c) T-3 and B-3 Series



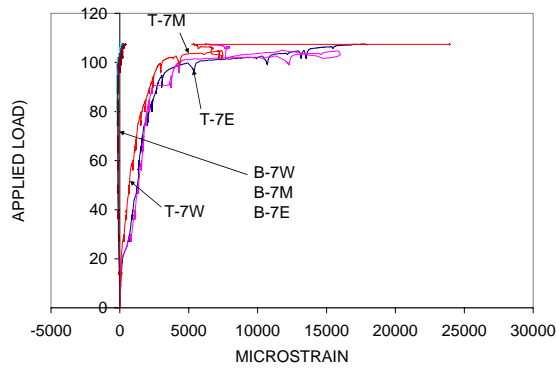
(d) T-4 and B-4 Series



(e) T-5 and B-5 Series



(f) T-6 and B-6 Series



(g) T-7 and B-7 Series

Figure F.4 Strain of Reinforcement Measured from Strain Gages